UNIVERSITÀ DEGLI STUDI DI PADOVA

Dipartimento di Fisica e Astronomia

Corso di Laurea in Fisica

Tesi di Laurea Magistrale

Diagnostics for negative ion source NIO1

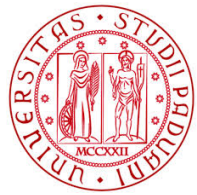

Relatore:
Dr. Gianluigi Serianni

Correlatori:
Dr. Marco Cavenago
Dr. Roberto Pasqualotto

Controrelatore:
Dr. Enrico Fagotti

Candidato:
Alessandro Mimo
matricola: 1058019

16 Settembre 2014 - A.A. 2013 - 2014

Abstract

The development of Neutral Beam Injectors (NBI) as auxiliary heating systems for ITER, the experimental reactor that will be realized in Cadarache (France), is a fundamental topic of the fusion science research in the last decades. For this purposes much effort is being to improve the understanding of the physics of negative ion beams and sources.

This thesis deals with the negative ion source NIO1, developed at Consorzio RFX in collaboration with INFN laboratories in Legnaro (Padova), in particular concerning the design, development and setup of some of the diagnostics for the first operation of the NIO1 source. The contents of this thesis are shortly summarised herebelow.

In *Chapter 1* the principles of fusion reactors are presented, discussing the need of additional heating systems: the Neutral Beam Injector and the negative ion source working principles are briefly described. In *Chapter 2* an overview of the NIO1 experiment is given, with particular focus on both the source and the beam diagnostics with which it is provided. In *Chapter 3* the conceptual design of the laser asborption spectroscopy for measuring cesium density is developed, defining the parameters of the optical system. The limits of this diagnostic are identified and evaluated by means of numerical simulations and corrective strategies are proposed. *Chapter 4* describes the cooling system for both the source and the beam calorimeter, presenting some considerations about the thermocouples and their fastening methods. In particular a new solution in which the thermocouples are placed in direct contact with water is devised and a prototype is realized and tested. *Chapter 5* presents the activity performed for the development and the setup of the source optical diagnostics, that is the plasma light detection system and the optical emission spectroscopy. In *Chapter 6* the experimental setup used for the first operation of NIO1 source is described, in which air was used as filling gas. The measured data from the optical diagnostics is reported and the analysis is explained. Furthermore the obtained results about the estimated electron temperature and vibrational and rotational temperatures of nitrogen are discussed. Finally *Chapter 7* summarises the main results and presents some suggestions for the future work.

Sommario

Lo sviluppo degli iniettori di fasci di neutri quali sistemi di riscaldamento addizionali per ITER, il reattore sperimentale che verrà realizzato a Cadarache (Francia), è un argomento fondamentale per la ricerca in ambito fusionistico degli ultimi decenni. Molti sforzi sono stati profusi al fine di meglio comprendere la fisica delle sorgenti e dei fasci di ioni negativi.

Nella presente tesi vengono affrontati la progettazione, lo svilppo e la messa in opera di alcune diagnostiche per la prima operazione della sorgente di ioni negativi NIO1, sviluppata presso il consorzio RFX in collaborazione con i laboratori nazionali di Legnaro dell'INFN. I contenuti della tesi saranno brevemente riassunti nel seguito.

Nel *Capitolo 1* vengono presentati i principi alla base dello sviluppo dei reattori per la fusione nucleare, sottolinenado la necessità della presenza di sistemi di riscaldamento addizionali: sono quindi brevemente descritti gli iniettori di fasci di neutri e le sorgenti di ioni negativi. Nel *Capitolo 2* viene presentato l'esperimento NIO1 nel suo complesso, con particolare attenzione alle diagnostiche della sorgente e del fascio. Nel *Capitolo 3* è descritta la progettazione della spettroscopia laser ad assorbimento per la misura della densità del cesio, definendo i parameteri del sistema ottico. Le limitazioni inerenti a questa diagnostica sono state evidenziate e valutate attraverso simulazioni numeriche, ricercando di conseguenza delle strategie correttive. Il *Capitolo 4* descrive il sistema di raffreddamento sia per la sorgente che per il calorimetero del fascio, enunciando alcune considerazioni riguardo le termocoppie e i relativi metodi di fissaggio. In particolare è stata proposta e progettata una nuova soluzione che prevede il posizionamento delle termocoppie in diretto contatto con l'acqua: alcuni prototipi sono stati quindi realizzati e testati. Il *Capitolo 5* presenta l'attività svolta per lo sviluppo e l'installazione delle diagnotiche ottiche per la sorgente, ovvero il sistema di rivelazione della luce di plasma e la spettroscopia di emissione. Nel *Capitolo 6* è descritto il setup sperimentale utilizzato per la prima accensione e operazione della sorgente di NIO1 in cui è stata utilizzata aria come gas di riempimento. I dati raccolti dalle diagnostiche ottiche sono stati ivi riportati, esponendo inoltre le tecniche di analisi utilizzate. Inoltre vengono discussi i risultati ottenuti riguardo la stima della temperatura elettronica, nonché le temperature vibrazionali e rotazioni dell'azoto presente in aria. Infine il *Capitolo 7* riassume i risultati di tali attività e presenta alcuni suggerimenti per il lavoro futuro.

Contents

Chapter 1

Introduction

1.1 Nuclear fusion for energy

To meet the rapidly growing global energy demand, the search for new clean and sustainable sources is one of the biggest challenges that humankind will have to face in next decades. As a matter of fact the fossil fuels like coal, oil and gas are rapidly depleting and their combustion generates serious environmental consequences, such as greenhouse effect. A possible solution, which constitutes an important world research field, is represented by nuclear fusion, in which two ligth nuclei can fuse together forming a heavier nucleus if they are given enough energy to overcome Coulomb repulsion. The fusion reaction probability is related to the cross section, which depends on the energy of the reactants and on the type of reaction: fig. 1.2 shows the reaction rate for the three reactions deuterium-tritium, deuterium-deuterium and deuterium-helium 3. Due to the higher cross section at low temperature of deuterium-tritium reaction than the other two reactions, this is the most convenient and promising one for the realization of a nuclear fusion reactor.

$$^{2}\mathrm{H} +^{3} \mathrm{H} \rightarrow {}^{4}\mathrm{He}(3.5\mathrm{MeV}) + \mathrm{n}(14.1\mathrm{MeV}) \tag{1.1}$$

Deuterium is easily available in the environment and can be extracted for example from sea water, in which it is present in a concentration of $\sim$ 30mg/l. Tritium instead is not very abundant in nature but it can be produced by neutron impact on lithium, which is quite easily available in earth crust [1][2].

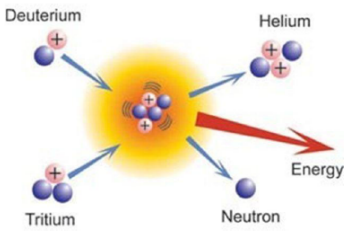

Fig. 1.1: Fusion reaction between deuterium and tritium.

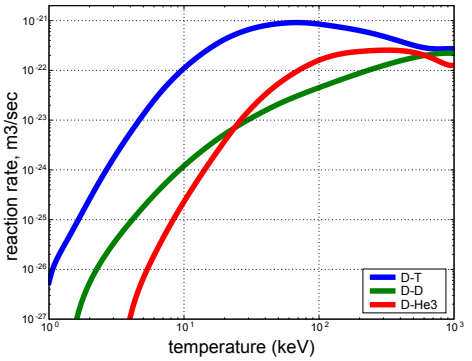

Fig. 1.2: Reaction rate of the reactions deuterium-tritium (blue), deuterium-deuterium (green) and deuterium-3He (red).

The reaction products, as can be seen in formula 1.1, are neutrons with an energy of 14.1MeV and helium-4 nuclei with an energy of 3.5MeV: in order to have a reaction rate high enough to produce a sufficient amount of energy, high values of temperature ($\sim$ 10keV) have to be achieved. At this temperatures the energy is high enough to ionize the atoms and the matter is in the plasma state, i.e. a ionized gas. The main goal to realize the nuclear fusion reaction in laboratory is to achieve the balance between the energy input, represented by the energy deposited to the plasma by α particles, produced in fusion reactions, and by additional heating systems, and energy losses, due to transport and radiation. The energy losses can be described by a parameter called energy confinement time τ_{E}:

$$\tau_{\mathrm{E}} = \frac{W}{P_{\mathrm{L}}} \tag{1.2}$$

where W is the total energy stored in the fusion plasma and P_{L} is the total power lost due to transport phenomena.

In order for the output energy not to be greater than the input energy (considering only that of α particles), the following condition has to be satisfied [3]:

$$n\tau_{\mathrm{E}} \geq \frac{12T}{\langle\sigma v\rangle E_{\alpha}} \tag{1.3}$$

where n is plasma density, T is temperature, $\langle\sigma v\rangle$ the fusion reaction rate and E_{α} the energy of the α particle. Since the function $\frac{T}{\langle\sigma v\rangle}$ is a fuction of temperature with an absolute minimum, by replacing its minimum value in eq. 1.3, the so called Lawson criterion is obtained:

$$n\tau_{\mathrm{E}} \geq 1.5 \cdot 10^{20} sm^{-3} \tag{1.4}$$

which, together with the requirement on temperature defines the conditions for a viable exploitation of nuclear fusion as an energy source. There are two possible techniques to achieve high values of $n\tau_{\mathrm{E}}$ product, depending on which of the two parameters is increased. In intertial confinement a laser is used to compress a mixture of deuterium and tritium, so that very high density is achieved for a very short time. The other possible way is to increase the energy confinement time by magnetically confining the plasma, which is composed of charged particles and thus sensitive to magnetic fields; closed magnetic field lines give the highest confinement. Hence toroidal machines were built around the world to test confinement and plasma production with different magnetical topologies: the most used and promising is the tokamak.

One of the advantages of this technolgy is its intrisic safety, with respect to nuclear fission:

- There is no possibility of runaway reaction: the ignition and maintenance of the plasma require so much effort that any change in the operating condition, for example due to a black out or other glitches, would simply turn off the reactions because they are no more substained. In addition the working pressure is much below the atmospheric pressure, so that in case of leakage, air enter the system and stops the reactions, preventing any risk of explosion.

- The radioactive pollution is still present, due to the activation of materials by high energy neutrons, but the life time of the radioactive waste is hundreds of years instead of thousands of years as for nuclear fission.

1.2 The ITER project

The ITER (meaning *the way* in latin) project started at the end of 1985, by an agreement between the European Union, the Soviet Union, the United States and Japan, with the aim of studying and developing the fusion energy with peaceful purposes. Other signatories joined the project later on, such as Republic of China and Republic of Korea in 2003 and India in 2005. The ITER agreement was signed in 2006 and the location selected for building the reactor was Cadarache, in southern France [2].

ITER is a toroidal machine based on tokamak magnetical confinement technology with which prove the feasibility of using nuclear fusion for energy production. The main goal for ITER is to achieve a positive balance between the fusion power produced and the input power. The fuel will be a mixture of deuterium and tritium, which are heated to a temperature of 10keV ($\sim$ 150 million °C) to form the

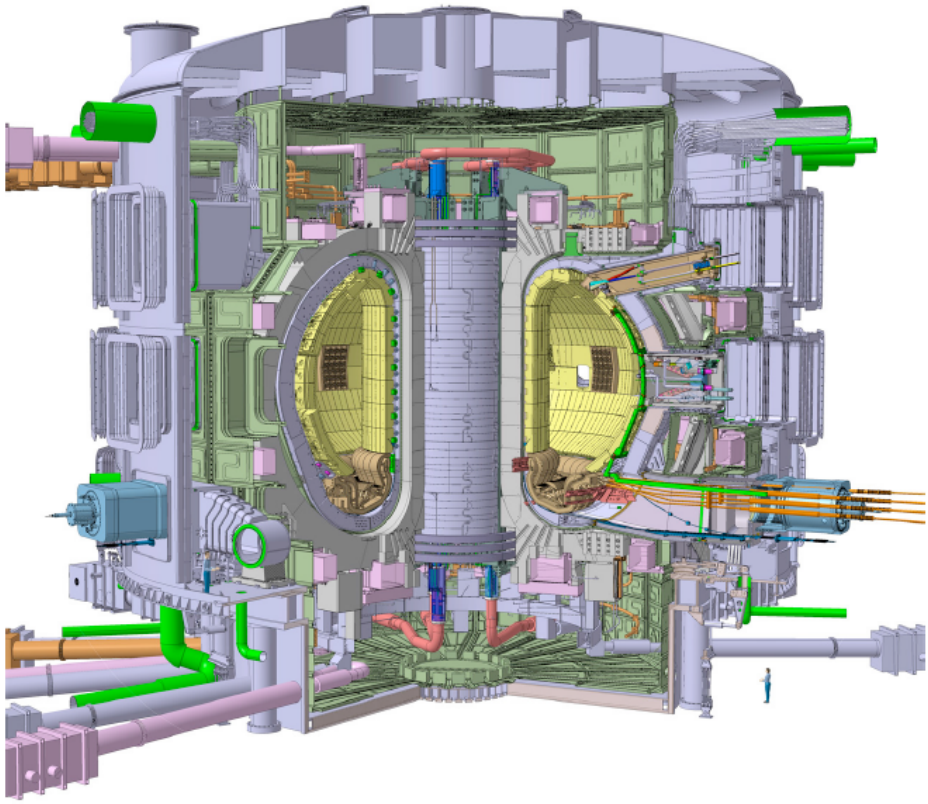

Fig. 1.3: Cutaway of ITER machine [2].

plasma. The magnetic field for the plasma confinement is mostly achieved by superconducting coils around the vessel and partly also thanks to the current driven in the plasma, which has also the aim of heating the plasma itself. The reactor is expected to produce a high fusion power of $\sim$ 500W with a duration up to 500s, with a gain factor at least of 10 (i.e. the ratio between fusion power produced and input power). In order to achieve the high tempertures required to start the fusion reactions, ITER will be provided with some external heating systems, since ohmic heating through plasma current is not enough to reach the input heating power required ($\sim$ 50MW). As a matter of fact the heating provided by ohmic effect is $\propto I_p^2 \cdot R_p$, where I_p is plasma current and R_p is plasma resistance: since plasma

ITER Parameters		
Fusion Power	500	[MW]
Power Amplification (Q)	≥ 10	
Major Radius	6.2	[m]
Minor Radius	2	[m]
Machine Height	26	[m]
Machine Diameter	29	[m]
Plasma Volume	837	[m^3]
Maximum toroidal field	5.3	[T]
Plasma Current	15	[MA]
Pulse length	≥ 400	[s]

Table 1.1: Main parameters of the ITER tokamak.

resistance decreases with increasing temperature, at high temperature ohmic heating becomes less effective. The additional heating systems are radio frequency heating, in which high frequency electormagnetic waves are used to deposit power in plasma, and neutral beam injection, i.e. the injection of high energy neutral particles which transfer their energy to the plasma by means of collisions.

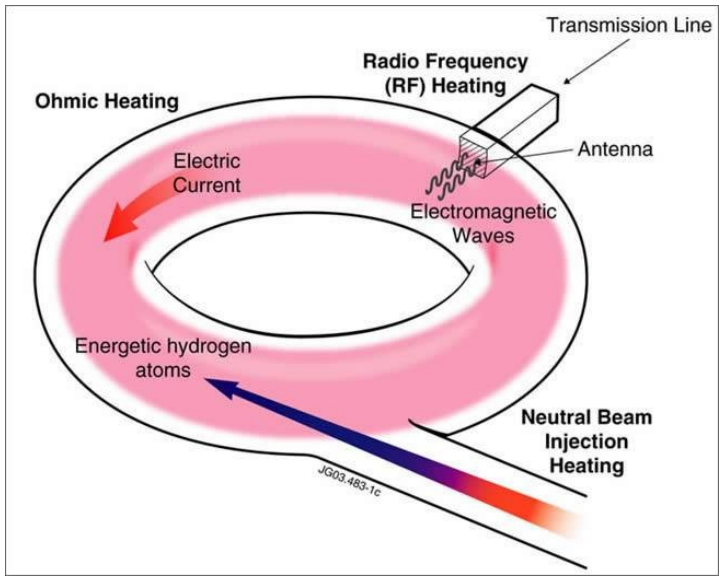

Fig. 1.4: Schematic of the different heating systems.

1.3 Neutral Beam Injector

The high-energy particles used to heat the plasma by beam injection have to be neutral, in order to overcome the strong magnetic field and penetrate into the plasma. Once the neutral particle is inside the plasma, it gets rapidly ionized through collisions and then confined by the magnetic field. Since the particle kinetic energy is large compared to plasma temperature, they deliver energy to the plasma particles by collisions.

The generation of fast neutral particles is achieved by producing high energy ions which are then neutralized, for example via charge exchange. The process can be subdivided in three principal steps:

- Generation of the high energy ion beam
- Neutralization of the ion beam
- Transport of the neutral beam to the plasma

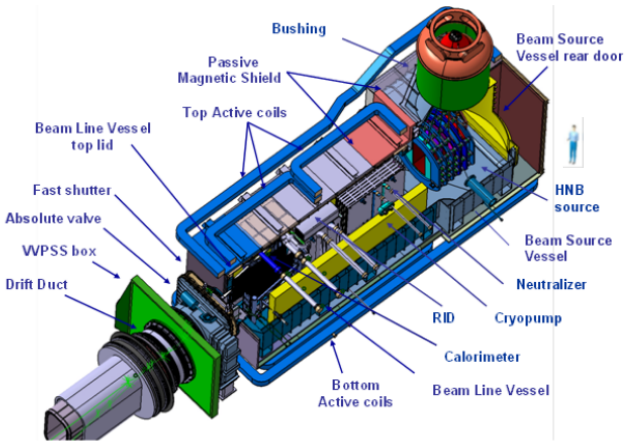

Fig. 1.5: Schematic of Neutral Beam Injector.

The production of the neutral beam by neutralizing positive ions cannot be achieved at high energy, since the charge exchange cross section falls down for energy greater than 100keV/nucleon, as shown in fig. 1.6. Therefore negative ions have to be used in order to maintain a high neutralization efficiency ($\sim 60\%$) also at higher energy (1MeV/nucleon). However H^- and D^- ions are very difficult to produce and accelerate avoiding substantial losses because of the low binding energy of the additional electron (0.75eV). Consequently, the study of negative ion

sources is very important in order to develop neutral beam injectors with energies up to 1MeV.

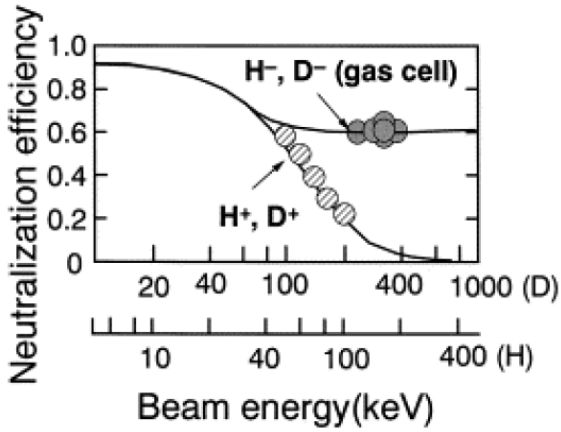

Fig. 1.6: Neutralisation efficiency as a function of beam energy for positive and negative ions [4].

1.4 Negative ion sources

The negative ions accelerated to create the beam are generated inside an ion source, whose type and specifications determines the characteristics of the beam. The ions generated are then extracted from the source thanks to an acceleration system, i.e. a series of grids biased at different electric potential. To ensure a beam delivered power of 16.7MW, which is the requirement for ITER, a 40A D^- ions current has to be extracted. In order to achieve such high current with reasonable size of extraction area, the current density is required to be $\sim 200 A/m^2$ [5].

The negative ion sources can be divided into two types depending on the way in which plasma is formed:

- *Arc driven sources*, the background gas is ionized by striking and electrical arc between the source body, acting as anode, and some filaments (hot catodes).
- *Radio Frequency driven sources*, in which a coil wound around the source wall is used to generate an inductive discharge. Due to the high-frequency electromagnetic waves emitted by the coil, acting as an antenna, the free electrons present in the source gain enough energy to ionize the background gas forming the plasma.

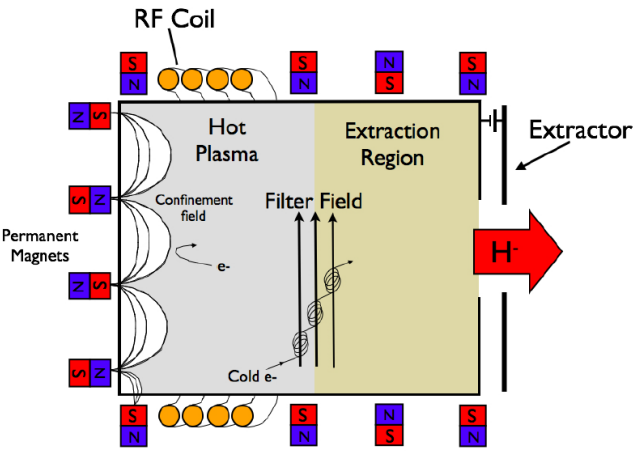

Fig. 1.7: Schematic of an RF ion source. Note the filter field to prevent hot electrons reaching the extraction region.

The RF sources were preferred for the ITER Neutral Beam Injector since they present some important advantages with respect to the arc driven, i.e. there is no need of frequent change of the filaments and there are no problems related with the pollution of plasma by tungsten consumption via evaporation and sputtering [6].

The plasma confinement is usually achieved by permanent magnets in the source wall, arranged in a multipole configuration, decreasing losses and increasing efficiency.

A negative ion is formed when an atom or a molecule captures an electron into an electron affinity level. There are two different physical mechanisms responsible for this, depending on the source of the captured electron: volume production, if the atom or molecule captures a free electron of the plasma itself; surface production, in which the electron is shifted from the conduction band of a metal surfaces surrounding the plasma [7][8][9].

1.4.1 Volume production

Volume production is supposed to proceed along these two steps [10]:

- Excitation of molecule to vibrational state by collision with high energy electrons

$$H_2 + e_{fast} \rightarrow H_2^* + e \tag{1.5}$$

- Dissociative attachment to form the negative ion

$$H_2^* + e_{slow} \rightarrow H^- + H_0 \tag{1.6}$$

During the production process there are also some destruction processes of the negative ions, i.e.:

- Electron detachment:

$$H^- + e \rightarrow H^0 + 2e; \tag{1.7}$$

- Mutual neutralization:

$$H^- + H^+ \rightarrow 2H^0; \tag{1.8}$$

- Associative detachment:

$$H^- + H^0 \rightarrow H_2 + e \tag{1.9}$$

For temperature above 1eV the dominant destruction process is the electron detachment. In fig. 1.8 the reaction rate for electron detachment (ED) and dissociative attachment (DA) is plotted: it can be seen that DA is quite insensitive to temperature variations while ED rapidly decreases with decreasing electron temperature. For this reason the negative ion sources are equipped with a so-colled magnetic filter, in which the magnetic field is directed parallel to the grid (fig. 1.7) and acts as an energy filter, so that slow electrons, which are more collisional, can diffuse perpendicularly to the magnetic field more easily than high energy electrons. In such a way, near the extraction region, the plasma density is increased and the electron temperature lowered, so as the ED ion destruction process is suppressed, resulting in an increased negative ions density.

1.4.2 Surface production

The surface production process is based on the shifting of an electron at the Fermi level in the conduction band of the metal surface of the suorce into an affinity level of an atom or molecule approaching the surface. The process in which an incident positive ion is reflected and converted to a negative ion is called secondary negative emission[11]. The efficiency of this conversion process can be strongly enhanced if the work function of the surface is lowered: in such a way the energy of the Fermi level of the metal is comparable to the electron affinity of the atom and electrons can tunnel.

In general the work function of a metal surface is lowered by depositing on it a material with a low work function. Cesium is the element with the lowest work function (1.81eV) [12]. The minimum value of the work function of a metal surface covered with cesium is given by the following equation [12]:

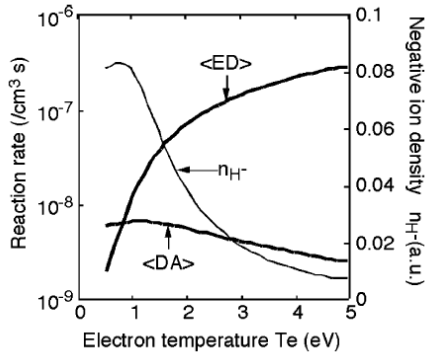

Fig. 1.8: Reaction rates of negative ion volume production (Disocciative Attachment) and ion destruction by Electron Detachment. The estimated negative ion density is shown in the plot [6].

$$\phi_{min} = 0.62(V_i + E_a) - 0.24\phi_0 \tag{1.10}$$

where ϕ_0 is the intrinsic work function of the metal, V_i is the first ionization potential of the covering matherial and E_a its electron affinity. For the case of cesium, the sum $V_i + E_a$ is the lowest of all elements, i.e. 4.35eV. In fig. 1.9 the

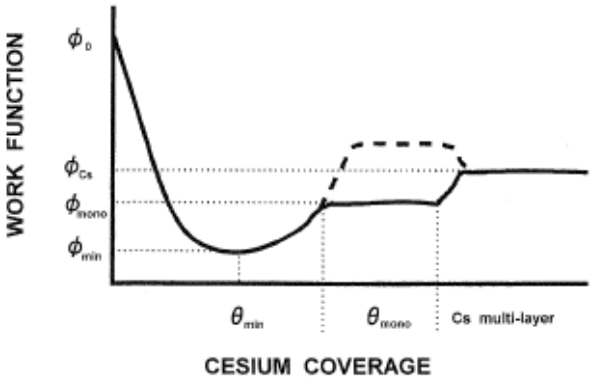

Fig. 1.9: Work function vs. cesium coverage [12].

work function of a metal is plotted as a function of the cesium coverage. With no cesium coverage the metal surface has its intrinsic work function, i.e. ϕ_0, but as

cesium is deposited the work function strongly decreases with increasing coverage, reaching a minimum for a value of θ of about 0.6 monolayers. At this point, increasing the cesium coverage the work function increases too, till it reaches the value of ϕ_{Cs} if cesium-multilayer is produced. Therefore in order to minimize the work function it is important that cesium coverage is under one monolayer: since at ambient temperature cesium-cesium bonding is very weak with the respect to metal-cesiumm a monolayer can be in principle achievable, but due to difficulties in having a controlled deposition on the surface and due to the fact that during plasma phase cesium is redistributed, the effective work function will be greater than that of a cesium monolayer.

1.5 Acceleration system

Once the negative ions are generated in the plasma, they have to be extracted in order to form the ion beam. As a matter of fact the plasma generator acts as a charged particle reservoir from which ions are extracted and accelerated by the so-called extraction system. This system determines the beam properties, such as ion currents and beam profile, i.e. it has the task of adapting the plasma generator to following beam transport system. The simplest type of extraction system is the diode type [12], consisting in two separate electrodes: the electrode facing the plasma is the extraction electrode which is negatively biased with respect to the other electrode. In such a way the potential difference between the two electrodes

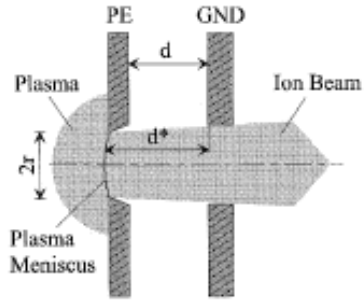

Fig. 1.10: Sketch of a simple diode type acceleration system [12].

generates an electric field, which is responsible for extraction and acceleration of the ions. The extraction current is either limited by emission or by space charge: in the latter case, if the amount of charges produced at the emitter (PE) increases, the charges travelling towards the collector (GND electrode) accumulate until their space charge is no more negligible, resulting in a screening of the electric field

experienced by the charges and determining the maximum value of current flowing through the diode. The Child-Langmuir law can therefore be used in order to calculate the emission current density (assuming a planar and infinite emission area):

$$j_{CL} = \frac{4}{9}\epsilon_0\sqrt{\frac{2e\zeta}{m}}\frac{1}{d^2}U^{3/2} \tag{1.11}$$

where ϵ_0 is vacuum permittivity, ζ is the ion charge state, m the ion mass, d the gap between electrodes, U the potential drop. Considering a cylindrically-symmetric extraction system, the integration of eq. 1.11 gives the total ion beam current:

$$I_{CL} = \frac{4}{9}\pi\epsilon_0\sqrt{\frac{2e\zeta}{m}}S^2U^{3/2} \tag{1.12}$$

where S is the aspect ratio, i.e. r/d and r the radius of the hole in the extraction electrode. The remarkable thing observed in eq. 1.12 is that the ion current is proportional to $U^{2/3}$ by the proportionality constant called perveance:

$$P = \frac{I}{U^{3/2}} = \frac{4}{9}\pi\epsilon_0\sqrt{\frac{2e\zeta}{m}}S^2 \tag{1.13}$$

The current density given by eq. 1.11 depends on the plasma density at the plasma meniscus. All ions with a small energy component in z direction are able to leave the plasma: the shape of the plasma meniscus therefore reflects the condition that the space-charge limited current density equals the ion current denisty. Hence the distance $d^\star$ between plasma meniscus and ground electrode adjusts so that the electric field strength at the plasma meniscus is zero. If the plasma density

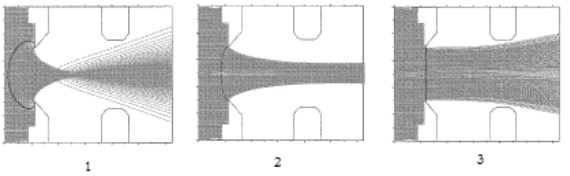

Fig. 1.11: Simulation for three different values of plasma density. From left to right $N_1 < N_2 < N_3$ [12].

is too low (N_1 in fig. 1.11) the distance d increases and the emitting area is concave shaped. If the plasma density is too high (N_3) the distance decreases and the emitting area might also be convex. Case two in fig. 1.11 is the most important because of the minimum divergence of ion beam trajectories. In order to increase the maximum current with respect to the optimal value according to

the Child-Langmuir law, while keeping as low as possible the beam divergence, more sophisticated extraction systems are used, for example the triode type, in which a third electrode is placed between the electron facing the plasma (plasma grid) and the ground electrode (grounded grid).

Chapter 2

NIO1 experiment

The NIO1 project consists of an RF inductively coupled ion source, capable of producing a negative ion beam accelerated up to 60kV, arranged in 9 beamlets with a nominal operative current of 15mA of H^- each, with the purpose of providing a test and training facility operating in condition similar of larger ion sources for Neutral Beam Injectors [13][14][15][16]. In this chapter a description of the apparatus will be given, with particular attention in section 2.2 and 2.3 to the source and beam diagnosics.

Fig. 2.1: Picture of NIO1 experiment.

2.1 Overview of the apparatus

The NIO1 apparatus is subdivided in three main parts:

- the source, in which plasma is generated by radiofrequency;
- the accelerating column, in which negative ions are extracted from the source and accelerated by a voltage drop between the grids;
- the diagnostics tube, in which diagnostics can be placed for the study of beam parameters.

The source consists of a cylinder composed by disk assemblies, with permanent magnets on the wall in order to provide an m = 7 multipole field for plasma confinement. The walls are water cooled by five independent circuits, four for the side wall and one for the rear, as it will be described in chapter 4. The RF power is coupled to plasma by a 7 turn coil which is wound around the source wall, made of 6mm outer diameter copper tube so that it can be water cooled.

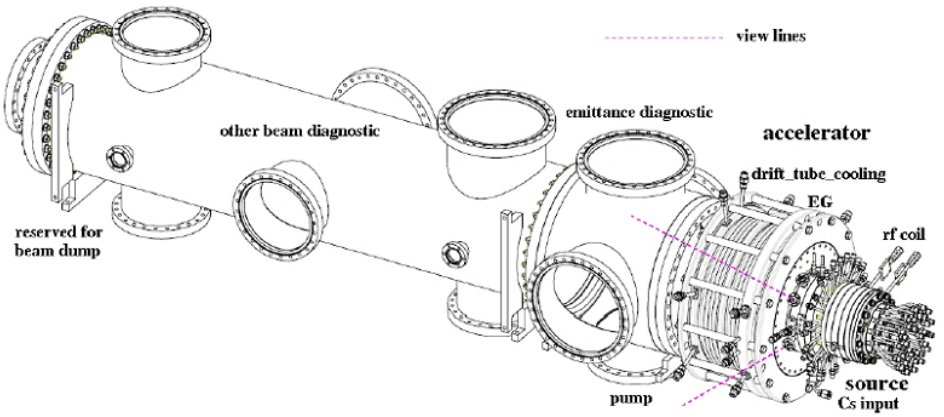

Fig. 2.2: Schematic of NIO1 apparatus.

The source is provided with a port for pressure gauge and a total of eight vacuum windows, four in the side next to plasma grid, and four in the back, for optical diagnostics, an input flange for evaporating cesium and a flange for a pressure gauge (see fig. 2.3 and 2.4).

The accelerator column consists of five grids:

- *Bias plate*, which can be polarized with respect to the source;
- *Plasma grid*, isolated from the source and biased up to some tens of volts with respect to the source which is held at -60kV;

- *Extraction grid*, at -51kV to regulate the current of extracted ions and stop the electrons deflected by permanent magnets installed onto grid itself;

- *Post acceleration grid*, at ground potential;

- *Repeller grid*, which can be positively biased up to 150V to repel positive ions, optimizing space charge compensation.

The plasma grid has 9 apertures, 8mm diameter, arranged in a 3 x 3 matrix, with a spacing between the center of two nearby holes equal to 14mm. The magnetic filter field is achieved thanks to a current flowing through plasma grid and bias plate.

Finally, the diagnostic tube, at ground potential, is provided with some CF ports for the pumping system and for beam diagnostics, for which a detailed description will be given in section 2.3.

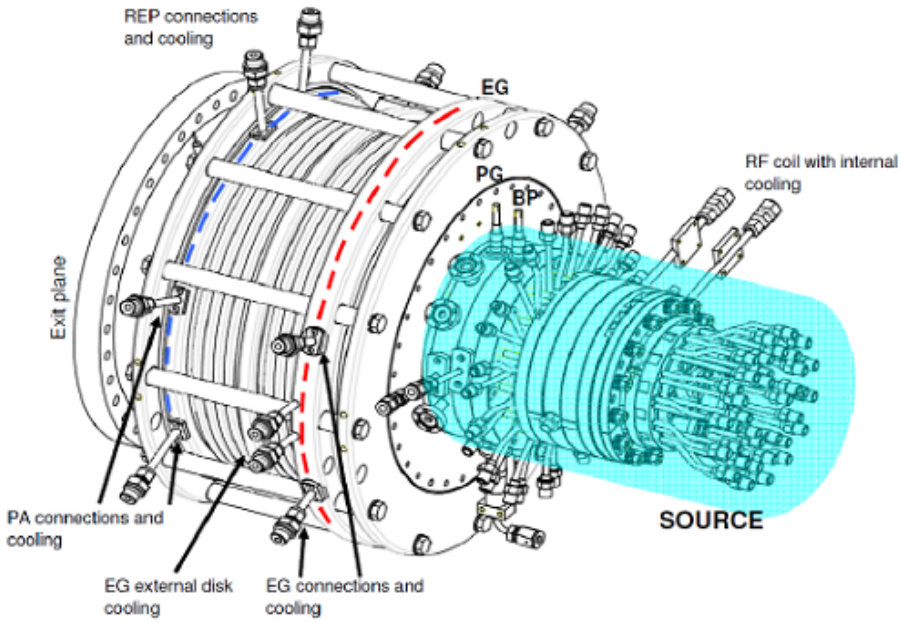

Fig. 2.3: Schetch of the source and of the accelearation system of NIO1.

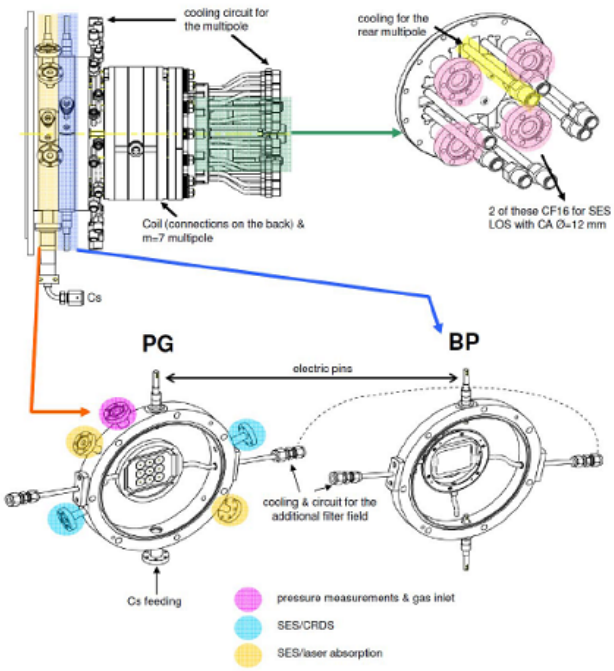

Fig. 2.4: Schematic of the source and grid cooling system and optical viewport.

2.2 Diagnostics of the source

The diagnostics of NIO1 source has the aim to study the parameters of the generated plasma. It involves the following systems:

- Optical emission spectroscopy, to measure plasma parameters such as electron temperatures and density, neutral and negative ion temperature;
- Plasma light detection, to identify plasma ignition and failures and to measure the total plasma light intensity;
- Cavity ringdown spectroscopy, to determine the negative ion density produced in the extraction region of the source;
- Laser absorption spectroscopy, to monitor cesium density in the chamber;
- Calorimetry, to have an estimate of the power deposited on material surfaces; part of this system can be used for security purposes.

The first two of these diagnostics were developed and tested during this thesis activity and will be further explained and described in detail in chapter 5. NIO1 is not yet provided with the other diagnostics listed: a design of a laser absorption spectroscopy apparatus was developed during this work and presented in chapter 3). Calorimetry of the source was another subject treated in this thesis, for which some considerations are presented in chapter 4.

2.2.1 Optical emission spectroscopy

In fig. 2.4 the optical ports that can be used for source emission spectroscopy are shown. NIO1 is provided with two lines of sight parallel to plasma grid and 26mm far from it, which can be used for source emission spectroscopy as well as for cavity ringdown and laser absorption spectroscopy; two more lines of sight are perpendicular to plasma grid and can be used for source emission spectroscopy and photometry. The lines of sight in the rear of the source crosses the driver along its axial direction, and hence they are no redundant with the other ones placed in the region near the plasma grid. In case that the most emissive region is the driver, using this rear lines of sight the plasma parameter in the driver can be measured.

The description of the optical system and the work done during the thesis activity for the set-up of emission spectroscopy will be presented in a dedicated section of chapter 5. From the analysis of source emission spectroscopy it is possible to obtain some fundamental parameters for optimizing negative ion formation in the plasma. The easiest use of source emission spectroscopy is line identification, which allows to monitor the presence of impurities, such as copper, due to sputtering or arcing on the metal surfaces. Also the monitoring of cesium by its line emission at 455.5nm and 852.1nm is very important; indeed, as described in section 1.4.2, cesium abundance controls the efficiency of negative ion production via surface processes. Moreover it is very important for the optimization of the source to measure plasma paramters, i.e. the temperature and density of electrons, gas vibrational and rotational temperatures as well as negative ion density. In the first experimental operation performed in this thesis work air was used as the filling gas, for the reasons explained in chapter 6, where also the data analysis and the first results will be presented. However NIO1 is designed to work with hydrogen as filling gas and so in the following of this section the measurement methods for the determination of the parameters of a hydrogen plasma by means of optical spectroscopy will be described.

The determination of electron temperature and electron density for the hydrogen plasma can be achieved by means of the line ratio method applied to the Balmer series[17]. The line emission for atomic hydrogen is correlated with the population density of the electronically excited state, which depends on electron temperature and density:

$$\epsilon_{pk} = n_H(p) A_{pk} \tag{2.1}$$

where n_H is the population density of atomic hydrogen in the excited state (with quantum number p) and A_{pk} is the transition probability. This dependence can be computed with the so-called collisional radiative model, which balances collisional and radiative processes for all electronic states and it is used in non-equilibrium plasmas (e.g. low pressure and low temperature hydrogen plasma).

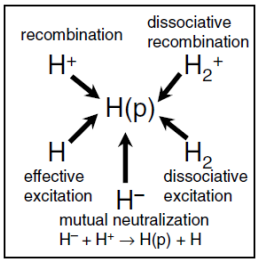

Fig. 2.5: Different processes involved in the population of excited states of atomic hydrogen [17] .

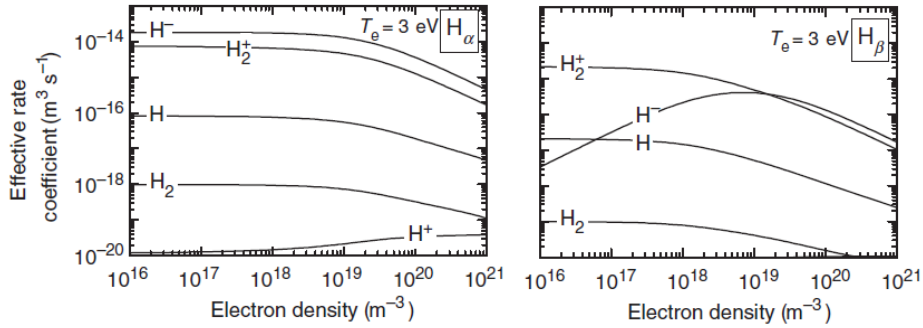

Fig. 2.6: H_α and H_β effective emission rate coefficients for different excitation processes as function of electron density [17] .

Taking into account the different processes which contribute to population of an excited state of atomic hydrogen, as shown in fig. 2.5, the following balancing formula can be obtained:

$$\begin{aligned} n_H(p) =& n_H n_e R_H(p) + n_{H^+} R_{H^+}(p) + n_{H_2} n_e R_{H_2}(p) \\ &+ n_{H_2^+} n_e R_{H_2^+}(p) + n_{H^-} n_{H^+} R_{H^-}(p) \end{aligned} \tag{2.2}$$

where the five population coefficient $R_s(p)$ can be calculated by the aforementioned CR model. Combining the eq. 2.1 and 2.2 and defining the effective emission rate coefficient as

$$X_{pk}^{eff,s} = R_s(p) A_{pk} \tag{2.3}$$

where A_{pk} is the Einstein coefficient, the line emissions can be computed as following:

$$\begin{aligned} H_M = n_H n_e \Bigg[& X_{H_M}^{eff,H} + \frac{n_{H^+}}{n_H} X_{H_M}^{eff,H^+} + \frac{n_{H_2}}{n_H} X_{H_M}^{eff,H_2} \\ & + \frac{n_{H^+}}{n_{H_2^+}} X_{H_M}^{eff,H_2^+} + \frac{n_{H^-}}{n_H} X_{H_M}^{eff,H^-} \Bigg] \end{aligned} \tag{2.4}$$

where M stand for α,β,γ,... . For the typical plasma conditions of negative ion sources, by computing the contributions of the different processes in eq. 2.4 it can be observed that Balmer line emission and their line ratio depend on electron density, electron temperature and density ratio H^-/H.

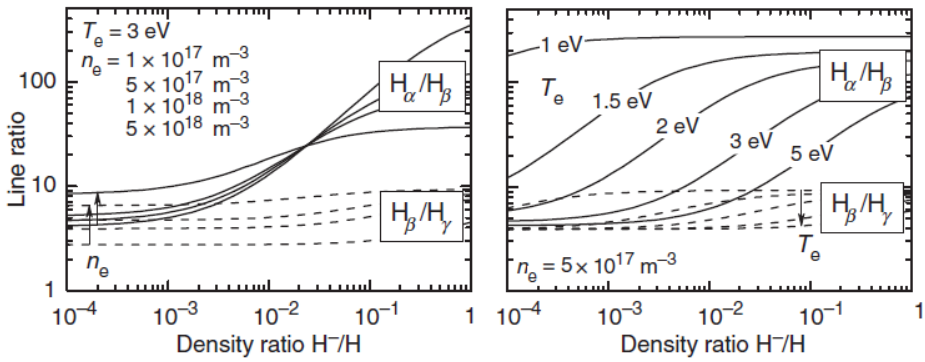

Fig. 2.7: Line ratio H_α/H_β and H_β/H_γ as function of denisty ratio H^-/H [17] .

In fig. 2.7 line ratios H_α/H_β and H_β/H_γ are shown as a function of density ratio H^-/H for different values of electron density and temperature. The line ratio

H_β/H_γ is independent from the density ratio H^-/H and sensitive to electron temperature. Instead the ratio H_α/H_β is strongly sensitive to the density ratio H^-/H in the condition $H^-/H > 10^{-3}$. In order to obtain also the value of negative hydrogen ion density and not only the ratio, the knowledge of neutral idrogen density is needed. For this purpose the H_γ line is used, since the dominant excitation path for this line is due to atomic hydrogen [17]:

$$H_\gamma = n_H(5)A_{52} = n_H n_e X_{H_\gamma}^{eff,H}(T_e, n_e) \tag{2.5}$$

By knowing the electron temperature is then possible to obtain the value of the effective rate emission coefficient, and then to compute the value of n_H. Therefore, by measuring the line ratios H_α/H_β, H_β/H_γ and the emission line H_γ, plasma parameters such as electron density, electron temperature, density ratio H^-/H and H^- density can be monitored.

The vibrational and rotational temperature of H_2 can be calculated using the Fulcher band spectrum, i.e. the roto-vibrational transitions of hydrogen molecules in the range 590-640nm. Since the roto-vibrational band has to be resolved in order to carry out the measurement, a spectrometer having a wavelength resolution under 60pm is mandatory [18] [19].

2.2.2 Cavity ring down spectroscopy

The aim of cavity ring down spectroscopy (CRDS) is the determination of negative ion density (H^-) produced in the extraction region of the source. The CRDS technique is used to perform highly sensitive absorption measurements: it consists of a cavity, made by two highly reflecting mirrors mounted on two collinear vacuum windows, into which a laser pulse is injected [20] [21]. The laser pulse is then reflected back and forth by the two mirrors and absorbed by the medium in the chamber. Since the mirrors are not exactly 100% reflecting, the light exiting from one of the mirror can be detected. Let the mirror have a reflecting coefficient R, then the transimission coefficient is:

$$T = 1 - R - A \tag{2.6}$$

where A includes the losses due to scattering and mirror coatings. If in the cavity there is an absorbing medium with absorption coefficient α, the intensity of the light after n round-trips will be:

$$I_n = \left[R\mathrm{e}^{-\alpha L}\right]^{2n} I_0 = I_0 \mathrm{e}^{2n\left[lnR - \alpha L\right]} \tag{2.7}$$

where L is the length of the cavity. Since the mirror are highly reflecting, $R \sim 1$ and then $lnR \sim R - 1 = -T + A$, leading to the expression:

$$I_n = I_0 \mathrm{e}^{-2n[T+A+\alpha L]} \tag{2.8}$$

The time for n round-trips is $t_n = \frac{2nL}{c}$, from which n can be derived as function of time, i.e. $n = \frac{tc}{2L}$. Substituting in eq. 2.8:

$$I(t) = I_0 \mathrm{e}^{-\frac{tc}{L}(T+A+\alpha L)} = I_0 \mathrm{e}^{-\frac{t}{\tau}} \tag{2.9}$$

Eq. 2.9 show that intensity decreases exponentially with time depending on a constant τ, called decay time:

$$\tau = \frac{L}{c(T+A+\alpha L)} = \frac{L}{c(1-R+\alpha L)} \tag{2.10}$$

This diagnostic has the aim of measuring H^- density, therefore the process that has to be considered is:

$$H^- + h\nu \rightarrow H + e \tag{2.11}$$

in which a negative hydrogen ion is converted in a neutral atom by photodetachment. In order to maximize the absortpion of laser light travelling in the medium, laser frequency has to be chosen so that cross section of the process is maximum.

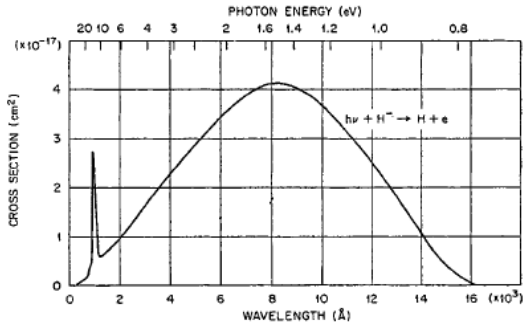

Fig. 2.8: Cross section of the photodetachment process for negative hydrogen ions H^- [22].

In fig. 2.8 the cross section of photodetachment for negative hydrogen ions is shown: it presents a broad peak around 800nm. Thus the proper laser type to be used is a YAG emitting at 1064nm. The determination of negative ion density is possible comparing the decay time in absence of plasma (i.e. the decay time due only to mirror losses, scattering, diffraction, etc.) and in presence of plasma, when

absorption increases. As a matter of fact in the absence of plasma the decay time is:

$$\tau_0 = \frac{L}{c\,(1-R)} \tag{2.12}$$

In order to know the value of negative ion density the absorption coefficient has to be determined, in fact the following relation holds:

$$\alpha = n_{H^-}\sigma_{H^-} \tag{2.13}$$

Using eq. 2.10 and eq. 2.12:

$$\left(\frac{1}{\tau} - \frac{1}{\tau_0}\right) = \frac{c\alpha d}{L} \tag{2.14}$$

from which α and then n_{H^-} through eq. 2.13 can be determined:

$$n_{H^-} = \frac{1}{\sigma_{H^-}}\frac{L}{cd}\left(\frac{1}{\tau} - \frac{1}{\tau_0}\right) \tag{2.15}$$

Therefore by measuring the light leaking from one of the mirror of the cavity firstly without plasma and then during operation, the decay times τ_0 and τ can be calculated fitting the signal with a negative exponential function, allowing the determination of negative ion density n_{H^-}.

2.3 Diagnostics of the beam

There are many parameters of the beam that are important and interesting to monitor, such as the direction of propagation, divergence, emittance and intensity profiles. In particular NIO1 will be provided with the following beam diagnostics:

- Visible tomography, to obtain the intensity profile of the beam (see section 2.3.1);
- Fast Emittance Scanner, which consists of an Allison scanner used to determine the emittance pattern, i.e. the ion phase-space density (see section 2.3.2);
- Beam Emission Spectroscopy, for measuring divergence of the beam thanks to the doppler shift of H_α radiation (see section 2.3.3);
- Instrumented calorimeter, with which information about intensity and emittance can be retrieved (see section 4.2);
- Ministrike, to obtain information about intensity profile by observing a CFC tile hit by the beam using a thermal camera (see section 2.3.4).

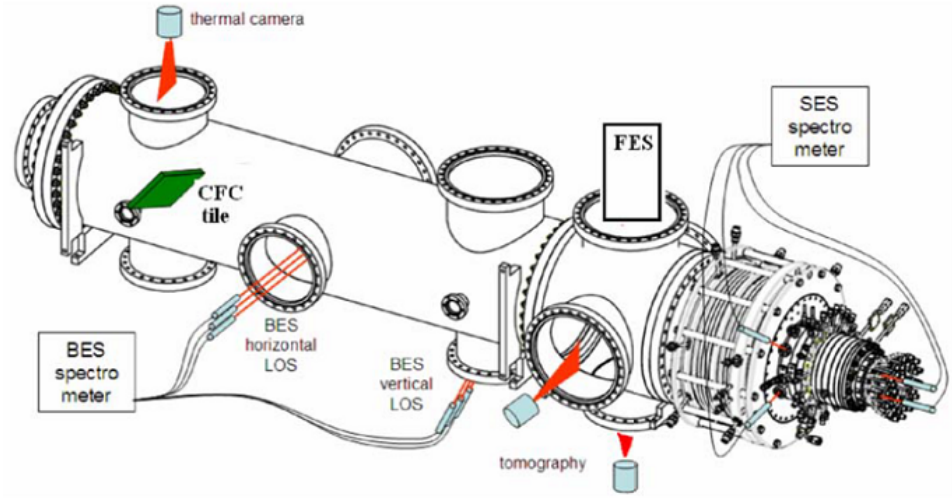

Fig. 2.9: Overview of NIO1 diagnostics [16].

2.3.1 Visible tomography

Visible tomography is a diagnostic used to obtain a two-dimensional intensity profile of the beam. Since the measured quantity is the integrated H_α radiation, an inversion algorithm is used to retrieve the spatial distribution of emissivity. Upon assuming that the background density is uniform across the beam, the 2D intensity profile can be calculated. One of the main advantages of this technique is that it is non intrusive, i.e. it can provide information about beam intensity and uniformity without interrupting it, as happens using an Allison scanner or a calorimeter. In such a way the beam can be monitored during operation with sufficient temporal resolution. In the experiment NIO1 the beam will be observed by two linear CCD cameras, each having its dedicated viewport with a fan of lines of sight and provided with its own objective lens. The CCD camera must have high quantum efficiency at H_α wavelength and a high dynamic range, in order to measure with high accuracy both low and hihh intensity signal detected by different lines of sight. Since this diagnostics is still to be designed for NIO1, the future work will consist in identifying and testing the CCD cameras and the characteristics of the optical systems.

2.3.2 Fast Emittance Scanner

Emittance is the property of a particle beam that characterizes the volume occupied by the beam particles in the phase space [23]. The phase space variables for a

particle are the three spatial coordinates together with the three components of momentum, i.e. x, px, y, py, z, and pz with time as the independent variable. The volume in this phase space is then:

$$V_6 = \int\int\int\int\int\int dx dp_{\mathrm{x}} dy dp_{\mathrm{y}} dz dp_{\mathrm{z}} \tag{2.16}$$

This quantity is used to describe a beam because unlike the physical dimensions of the beam, which may vary as the beam propagate, emittance is invariant in the absence of dissipative forces. In the transverse emittance only the two directions perpendicular to beam axis are considered. The transverse emittance plot can be obtained plotting the particle density in the phase space plane x - α_x, where α_x is the angle between the trajectory of the particle and the beam axis. An Allison scanner is an instrument used to measure the transverse emittance of an ion beam. It consists of a measuring head with two slits, the entrance slit and the exit slit, aligned and with a distance D between them (fig. 2.10) [15].

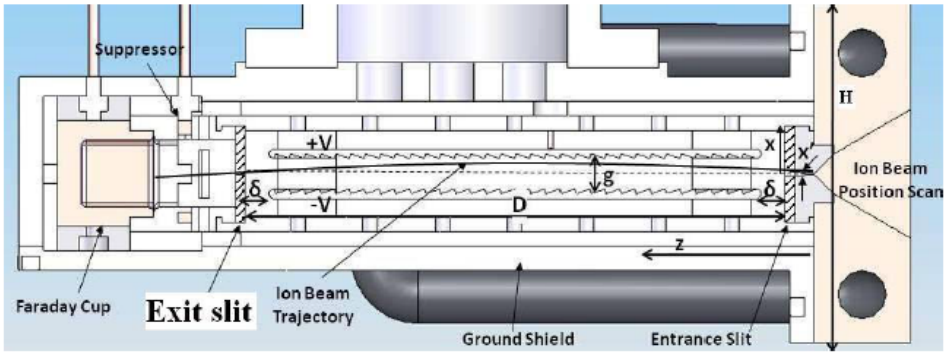

Fig. 2.10: Schematic of an Allison scanner [15].

Let x be the direction given by the axis of insertion of the scanner head and z the direction of propagation of the beam. The entrance slit is used to select the particle position x(t), determined by the instantaneous position of the slit. Between the two slits of the measuring head there are two parallel deflecting plates, biased with a voltage ramp varying with time V(t). Due to the electric field, the charged particle which entered the first slit is deflected by an amount $x_d(z) \propto V(t)$. As a matter of fact the electric field determines an acceleration for the particle:

$$a = -\frac{e}{m}\frac{V_d}{g} \tag{2.17}$$

where g is the gap between the plates and m the mass of the ion, and V_d is the voltage drop between the plates. Once the ion has crossed all the measuring head

it reaches the second slit and it passes it only if the condition $x_d\,(D) + x'D \sim 0$ is satisfied, i.e. the total deflection is zero. The total deflection is that due to the acceleration term plus that due to the angle α_x: equating this deflection to zero it is possible to obtain the relation between V_d and x'.

$$x' = \frac{D_\delta V_d}{4 g v_b} \tag{2.18}$$

where v_b is the voltage used to accelerate the ion beam and D_δ is the length of the deflecting plates. The particles which pass the slit hit a Faraday cup with a suppressor for electron secondary emission so that the measured current I(t) is the incoming ion current. Summing up, the position of the entrance slit selects the spatial coordinate of the ion x(t) and the voltage V(t) selects only the ions with x'(t) equal to that of eq 2.18: thus measuring the I(t) it is possible to obtain the ion phase-space density.

Plate spacing g	8	mm
Plate length D	100	mm
δ	5	mm
slit width s	5	mm
Max. defl. voltage	$\pm$ 0.43	kV
x' upper bound	$\pm$ 40	mrad
Slew rate	300	V/μs
maximum head speed	0.3	m/s
f bandwith	31	MHz

Table 2.1: FES design parameter [15] .

The FES paramters designed for NIO1 are reported in table 2.1. The voltage ramp of the deflecting plate is a symmetrical trianglular wave with a period of 66μs, and the sampling of V(t) should be at least 1MS/s. The available position to place the FES in NIO1 are in the NIO1 crossing pump at 0.46m from PG, at 0.97m and 1.47m from plasma grid, both with vertical and horizontal insertion axis. The determination of the slit widths are very impornat since they determine both the position and angular resolution. As for the I(t) acquisition system, the sampling rate is specified to be 240MS/s, so that fast acquisition is possible during beam crossing.

2.3.3 Beam emission spectroscopy

The beam emission spectroscopy is a very powerful diagnostics to measure divergence, uniformity and direction of propagation of the beamlets, as well as the fraction of ions neutralized in the accelerating system, without perturbing the beam

continuity [24]. The energetic ions interacts with the background gas in the chamber: these collisions produce excited neutral particles, which then emit photons due to de-excitation. The emission line considered is the H_α line, which appears to be Doppler shifted due to the velocity of the particle in the laboratory frame of reference and the Doppler shift is equal to:

$$\lambda' = \lambda_0 \frac{1 - \beta cos\,(\alpha)}{\sqrt{1-\beta^2}} \tag{2.19}$$

where λ' is the shifted wavelength, λ_0 the unshifted one, β the ratio between ion speed and speed of light and α is the angle betwen the de-excited neutral trajectory and the direction of observation. Since the beamlet of NIO1 are arranged in a 3x3 square matrix there are six lines of sigth available for BES and aligned with the beamlets, three horizontal and three vertical. Lines collected by the telescopes are focused into an optical fiber and the spectrum obtained by means of a grating spectrometer. Many beam parameters can be inferred measuring the Doppler shift of H_α and the width of the unshifted H_α peak which is always present due to de-excitation of background gas. The width of unshifted H_α peak is due to many contributions [25]:

$$\begin{aligned}\Delta\lambda^2 =& \Delta\lambda_I^2 + \Delta\lambda_N^2 + \left(\frac{\lambda_{zero}}{\sqrt{1-\beta^2}}\beta sin\,(\alpha)\right)^2 \left(\omega^2 + \epsilon^2\right) + \\ &+ \left(\frac{e\lambda_0}{mc^2\beta}\left(\beta - cos\alpha\right)\right)^2 v^2\end{aligned} \tag{2.20}$$

where $\Delta\lambda_I$ is the intrinsic width of the line, $\Delta\lambda_N$ the broadening introduced by the spectrometer, ω the angle with which the lens is seen by the emitting particle, ϵ the avarage divergence of the beamlets and v the voltage ripple of the grids. The value of α can be obtained with eq. 2.19 by measuring the Doppler shift in wavelength and β is determined by the accelerating voltage: thus measuring the unshifted peak width it is possible to obtain the divergence ϵ if all the other broadening factors are known. In addition information about uniformity can be retrieved comparing the integral of the Doppler shifted peak for different lines of sight.

2.3.4 Mini-STRIKE calorimeter

The measurement of the intensity profile of the beam can be achieved using a one-directionalcarbon fiber composite (CFC) tile used as beam target. The thermal conductivities of 1D-CFC tiles are not isotropic, as a matter of fact it is strongly enhanced in the direction of the thickness of the tiles (i.e. z-direction in fig 2.11, where a CFC tile is shown).

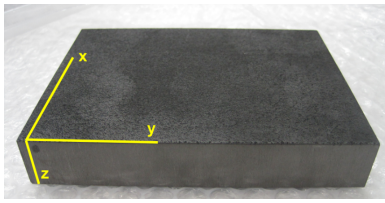

Fig. 2.11: CFC tile. The z direction is the one with enhanced thermal conductivity.

The tile are then exposed perpenduclarly to the beam, so that the beam direction is parallel to the high-conductivity direction of the tile. In such a way the thermal pattern is preserved during the transmission from the front to the rear side of the tiles: therefore, observing the tile with an IR thermal camera, it is possible to retrieve the intensity profile of the beam. Fig. 2.12 reports an image obtained by a thermal camera of mini-STRIKE, a test diagnostics consisting of two CFC tiles. Measurement were performed in BATMAN test facility at IPP (Institute für plasmaphysics) of Garching in 2012 [26]. Mini-STRIKE was realized to test the applicability of the CFC tiles for STRIKE, i.e. the Short-Time Retractable Instrumented Kalorimeter Experiment [27], one of the diagnostics of the neutral beam prototype SPIDER, now under construction in Padova. The same type of diagnostic might be implemented in NIO1 [16], in order to have a cross-checking of the beam intensity measurement achievable by other diagnostics, such as the instrumented calorimeter and the visible tomography.

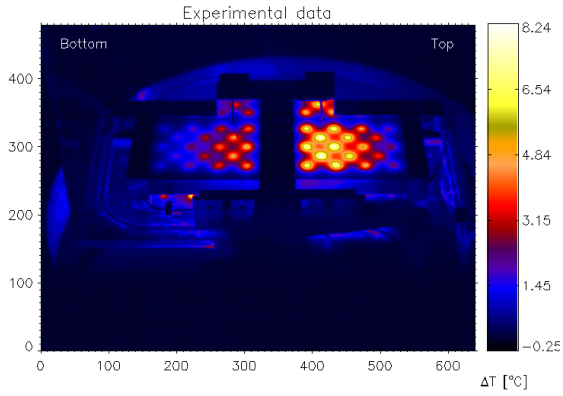

Fig. 2.12: Thermal image of mini-STRIKE obtained at BATMAN test facility (in 2014) [28] .

Chapter 3

Design of laser absorption spectroscopy apparatus

The experiment NIO1 will be equipped with a system to evaporate cesium in the chamber so that it can deposit on the grids, enhancing the negative ion production efficiency as described in 1.4.2: it is then very important to monitor cesium density for the optimization of surface conditioning. A possibile method that can be used is optical emission spectroscopy, which allows to measure cesium density detecting its spectral line at 852nm. It is worth noting however that this technique is sensitive to neutral cesium, since 852nm line is that of Cs I, but in plasma phase most of cesium is ionized. Another important disadvantage of optical emission spectroscopy is that it requires the presence of a plasma (to have emission) and the knowledge of plasma parameters, such as electron density and electron temperature. In order to determine cesium density also in the so called vacuum phase, i.e. with no plasma, laser absorption spectroscopy can be used, since it is based on the study of the aborsption spectrum of a laser tuned to a resonant transition of atomic cesium.

3.1 Resonant transition of cesium

The ground state of cesium is a $6^2S_{1/2}$ state and the first excited configuration is split in two states by fine structure: $6^2P_{1/2}$ and $6^2P_{3/2}$. The corresponding resonant transitions are the D_1 line at 895.3nm and the D_2 line at 852.1nm: the last one is the most suitable both for laser absorption spectroscopy and for optical emission spectroscopy due to its lower wavelength, for which detectors have a better sensitivity and also laser sources are more easily available.

The ground state is split in two levels by hyperfine structure with total angular momentum quantum number which is $F = 3{,}4$ and the excited state $6^2P_{3/2}$ is

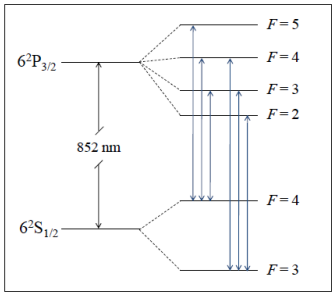

Fig. 3.1: D_2 energy level.

split into four hyperfine levels with $F = 2,3,4,5$. Taking into account the selection rules (i.e. $\Delta F = 0, \pm 1$), the D_2 lines have an hyperfine structure consisting of six lines. Because of Doppler broadening some of these lines overlap, resulting in the observation of only two resolvable peaks which can be considered Gaussian, with a wavelength distance between them of 24.1nm and the full width at half maximum, due to Doppler broadening, around 2pm at 1000K [29].

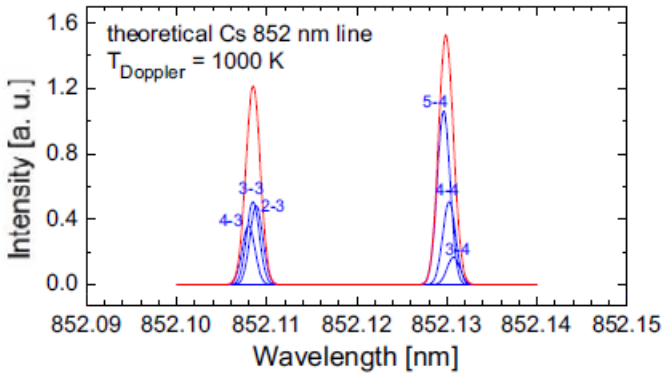

Fig. 3.2: Theoretical spectrum of 852nm Cs line at 1000K.

3.2 Theory of laser absorption spectroscopy

If a laser beam of spectral intensity $I(\lambda,0)$ passes through a uniform medium of length L, the spectral intensity of transmitted radiation is:

$$I(\lambda, L) = I(\lambda,0)\, exp\{-\tau(\lambda)\} \tag{3.1}$$

and τ is the optical depth:

$$\tau(\lambda) = \left(\frac{\lambda_0^4}{8\pi c}\frac{g_i}{g_k}A_{ik}\right) Ln_k P(\lambda) = \alpha P(\lambda) \tag{3.2}$$

where λ_0 is the center wavelength of the transition, A_{ik} the Einstein coefficient, g_i and g_k the degeneracies of the levels, n_k is the ground state density of cesium neutral atoms and $P(\lambda)$ is the normalized line profile of the transition, i.e.:

$$\int_0^\infty P_{line}(\lambda)\, d\lambda = 1 \tag{3.3}$$

Integrating equation 3.2 it is then possibile to obtain n_k:

$$n_k = \left(\frac{8\pi c g_i}{\lambda_0^4 g_k A_{ik}}\right)\frac{1}{L}\int_{line} \ln\left(\frac{I(\lambda,0)}{I(\lambda,L)}\right) d\lambda \tag{3.4}$$

On one hand the fact that this technique is sensitive to neutrals density is an advantage, because it can be used both in plasma phase and in vacuum phase, on the other hand it is important to keep in mind that cesium is heavily ionized in plasma phase and so values of density obtained only refer to the neutral population Equation 3.4 shows that density can be calculated simply by integrating the ratio between incident and transmitted spectral intensity, suggesting that there is no need of an absolute intensity calibration.

3.3 Apparatus for NIO1

During the thesis work the spefications of the laser absorption spectroscopy apparatus for NIO1 experimented were pointed out and in particular the optical system was designed, as shown in fig. 3.3. In order to carry on the integration in eq. 3.4, the laser source must be tunable in wavelength so that it is possible to measure the transmitted intensity spectrum. i.e. transmitted intensity for a range of wavelength scanning the lines of interest. A valid choice is a distributed feedback laser diode (DFB-0852-150) with a power of 150mW and tunable around D_2 cesium resonant transition between 851nm and 853nm: the coarse tuning is achievable through temperature modulation and the fine tuning is obtained thanks to current modulation. In order to modulate temperature and current a laser controller, such as Pilot PC500, is needed.

The light emitted by the laser is then collected by an optical fiber, coupled to a lens at the exit side, in order to create a collimated beam which is attenuated by a ND filter before crossing the medium. The transmitted light is then collected and focused into another optical fiber, reaching the detector. Available vacuum windows in the NIO1 source, for a line of sight parallel to the grids, have a diameter of 8mm,

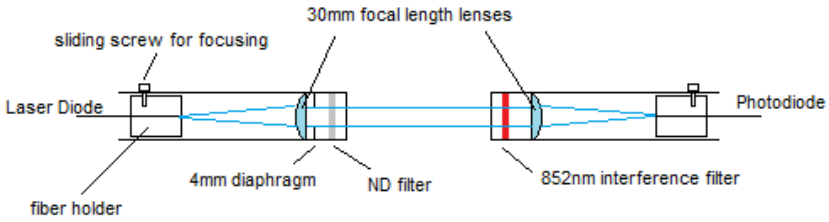

Fig. 3.3: Schematic of the apparatus.

so to avoid vignetting the laser beam diameter was chosen to be 4mm. Since the diameter of the optical fibers is 400 μm, i.e. $\frac{1}{10}$ of beam diameter, they cannot be regarded as point sources. In order to create an image of the fiber on the opposite side of the chamber and with a magnification factor $M \sim 10$, the proper value for the focal length of the lenses can be computed using lens equation:

$$f = \frac{q}{M-1} = 31.1mm \sim 30mm \tag{3.5}$$

where q is the distance between the two collinear windows. In order to be sure that all the transmitted light is collected by the fiber the f-number of the lens must be greater than the f-number of the fiber, which can be calculated from its numerical aperture $NA = 0.22$. The following calculation shows that this requirement is fulfilled for the 30mm focal length, 4mm diameter lens.

$$\begin{aligned} \left({}^{f}/_{\#}\right)_{fiber} &= \frac{1}{2NA} = 2.3 \\ \left({}^{f}/_{\#}\right)_{lens} &= \frac{f}{D} = 7.5 \end{aligned} \tag{3.6}$$

A passband interference filter centered at 852nm (with a FWHM of 10nm) has to be placed before the detector to avoid collecting light from plasma emission at other wavelengths. The detector will consist of a photodiode, producing a current proportional to the intensity of light collected, and a transimpedence amplifier, receiving as input the photocurrent and providing a proportional voltage as output.

3.4 Requirements for cquisition system and data analysis

The simultaneous acquisition of the output voltage of the photodiode amplifier together with the signal of the laser controller (driving the emission wavelength)

provide the reconstruction of the spectrum of transmitted intensity, which appears to be like in fig. 3.4.

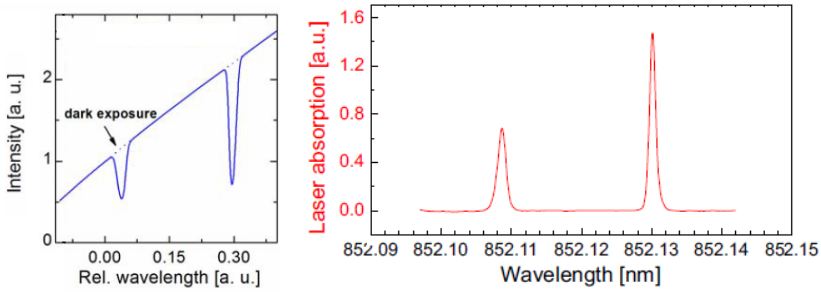

Fig. 3.4: Left: photodiode signal intensity as a function of tuned laser wavelength. Right: absorption signal.

The temporal resolution of the measurement is determined by the gain of the amplifier: with a lower gain a faster acquisition is achievable. However in order to decrease the gain of the amplifier it is necessary to increase the laser light intensity, so that an acceptable signal-to-noise ratio is maintained. As it will be explained further, some problems concerning depopulation of the ground state may arise from an excessively high light intensity, causing an underestimation of cesium density: to avoid this problem a compromise between gain and temporal resolution should be found. The distance between the two aforementioned peaks of D_2 transition is 24.1pm, so the wavelength scan of the laser should be $\pm$ 20pm around the center wavelength (i.e. a total span of 40pm). Since the Pilot PC500 laser controller has a 0.1mA current resolution and the laser tuning-current coefficient is 3pm/mA, the wavelength resolution of the tuning is 0.3pm: the points per spectrum to be acquired are then around 130 and assuming a desired frequency of acquisition of 25 spectra per second, it means 3000 points per second Using the PDA200C as transimpedence amplifier the maximum gain at which it still have a sufficient acquisition frequency is 10^6V/A, as can be seen in table 3.2.

Fitting the baseline of the spectrum far from the absorption dips it is possible to calculate $I(\lambda,0)$ and then the so-called absorption signal $\ln\left(I(\lambda,0)/I(\lambda,L)\right)$ (fig. 3.4). Using a fitting procedure instead of using a fixed value for $I(\lambda,0)$ (for example measured a priori in vacuum before evaporating cesium) is a better solution because in such a way any variation (due to instability of emission power of the laser, coating of the window determining a different absorption coefficient, etc.) is easily taken into account. The distance of the peaks is used for a relative wavelength calibration so that it is possible to integrate the absorption signal over wavelength obtaining, through eq. 3.4, an estimate of the cesium density.

Drive Current Output	
Output current range	0-500mA
Setpoint Resolution	0.1mA
Setpoint Accuracy	± 0.1% of FS
Noise:	<5μA RMS
Temperature coefficient:	<50ppm/Â°C
Short-Term Stability (1hr.):	<20ppm
Long-Term Stability (24hr.):	<50ppm
Drive Current Limit Setting	
Range	1-500mA
Resolution	0.1mA
Preregulator Voltage	
Adjustable:	0 - 7 V
External analog modulation	
Input Voltage Range:	-10V...+10V
Transfer function:	60mA/V
Bandwidth:	6kHz

Table 3.1: Pilot500 specifications.

Range	**Resolution**	**Accuracy**	**Gain**	**Bandwidth**
10mA	1μA	± 0.05% f.s.	$1 \cdot 10^3 V/A \pm 5\%$	500kHz
1mA	100nA	± 0.05% f.s.	$1 \cdot 10^4 V/A \pm 5\%$	250kHz
100μA	10nA	± 0.05% f.s.	$1 \cdot 10^5 V/A \pm 5\%$	70kHz
10μA	1nA	± 0.05% f.s.	$1 \cdot 10^6 V/A \pm 5\%$	20kHz
1μA	100pA	± 0.05% f.s.	$1 \cdot 10^7 V/A \pm 5\%$	5kHz
100nA	10pA	± 0.05% f.s.	$1 \cdot 10^8 V/A \pm 5\%$	1kHz

Table 3.2: PDA200C specifications.

3.5 Error sources

There are three important issues that can lead to uncorrected values of cesium density [30]:

1. Line saturation
2. Lower state depopulation
3. Laser background emission

These three error sources will be discussed in the following sections, presenting some considerations about the results of simulations carried on during the thesis

activity, in order to achieve a better understanding of the experimental conditions for which these phenomena could involve relevant problems for the measurement.

3.5.1 Saturation

In case of high absorption, the intensity of transmitted light rapidly decreases in the center wavelength determining a flattening and a broadening of the line profile. This effect may represent a real problem only in case of white light absorption spectroscopy, because the spectral resolution of the spectrometer used is much broader than the Doppler width, therefore the width of the lines is almost due to the spectrometer profile. In the case of laser absorption spectroscopy instead, the line width of the laser is much smaller and the line profile can be easily resolved, directly identifying saturation. To avoid this problem experiments should be carried on to determine the proper value for the incident intensity so that also for high density no flattening of the absorption profiles occurs. It has to be taken into account, however, that also the negative effects of depopulation increase with increasing light intensity.

3.5.2 Depopulation

The population of the lower state of cesium atoms is reduced by the excitation process provided by incident laser light, causing a significant reduction in the absorption and so an underestimation of cesium density. This phenomenum can be described by considering an intensity dependent absorption coefficent [31]:

$$k(\lambda) = \frac{k_0(\lambda)}{\sqrt{1+S_0}} \tag{3.7}$$

where k_0 is the absorption coefficient independent from intensity, i.e.

$$k_0(\lambda) = \frac{\tau(\lambda)}{L} \tag{3.8}$$

The intensity dependece in eq. 3.7 is due to the saturation parameter S_0, which is proprotional to the intensity

$$S_0 = \frac{2\sigma_0 I}{\hbar\omega A} = \beta I \tag{3.9}$$

where σ_0 is the resonant cross section, A the Einstein coefficient, ω the transition frequency and I the incident intensity. The absorption signal was simulated using the absorption coefficient of eq. 3.7 and then density estimated with the eq. 3.4, which does not take into account depopulation. In fig. 3.5 the ratio between the real density and the measured density is plotted as a function of real density

used in simulation, for different values of intensity. It is evident that the effect of depopulation is higher for lower densities, as expected.

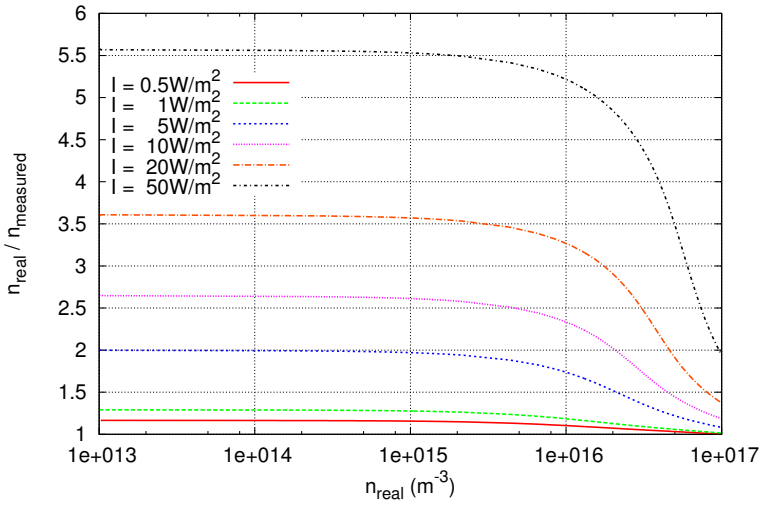

Fig. 3.5: Ratio between the real density used in simulations and the corresponding measured density without taking into account saturation.

For this reason eq. 3.4 cannot be used to estimate density if a significant depopulation occurs, and a correction is therefore necessary. The intensity loss dI due to a path dx is:

$$dI = -Ik(\lambda)\,dx = \frac{-I}{\sqrt{1+\beta I}}k_0(\lambda) \tag{3.10}$$

which gives through integration:

$$\begin{aligned} &\int_{I(\lambda,0)}^{I(\lambda,L)} \frac{\sqrt{1+\beta I}}{I}dI = -\int_0^L k_0(\lambda)\,dx \\ &f[I(\lambda,L)] - f[I(\lambda,0)] = -\tau(\lambda) \\ &f[I] = 2\sqrt{1+\beta I} + \ln\left(\sqrt{1+\beta I}-1\right) - \ln\left(\sqrt{1+\beta I}+1\right) \end{aligned} \tag{3.11}$$

Integrating eq. 3.11 over wavelength:

$$n_k = \frac{4\pi c}{\lambda_0^4}\frac{1}{A_{ik}L}\int_{line}\{f[I(\lambda,L)] - f[I(\lambda,0)]\} \tag{3.12}$$

the corrected equation for the density is obtained. In case of low intensity the results from eq. 3.12 are in agreement with the ones given by the uncorrected eq.

3.4, as can be immediatly proved by a series expansion of the function $f[I]$.

There is a simple and qualitative experimental way to check if depopulation is affecting the measurement. Starting with a condition in which the cesium density is settled, e.g. in vacuum phase, if a variation in the measured density is observed by changing the incident light intensity (i.e. changing the grade of the ND filter), therefore the regime is intensity-dependent and the effect of depopulation is then evident.

3.5.3 Laser background emission

The laser diode emits light not only at the tuned wavelength, infact it presents a broadband background emission, whose intensity is certainly much smaller than that of the emission peak but which is alike collected by the photodiode (since the $\Delta\lambda$ of the interference filter is 10nm). In case of high absorption the emission peak of the laser is obviously reduced while the background baseline is not, determining a relevant offset in the photodiode current. The situation can be mathematically modeled as follows:

$$\begin{aligned} \frac{I_{measured}(\lambda, L)}{I(\lambda,0) + b(\lambda)} &= \exp\{-\alpha P(\lambda)\} + \frac{\int_{\Delta\lambda_{filter}} b(\lambda')\, d\lambda'}{I(\lambda,0) + b(\lambda)} = \\ &= \exp\{-\alpha P(\lambda)\} + B \end{aligned} \tag{3.13}$$

where $b(\lambda)$ is the spectral intrinsic baseline of the laser, and B is the consequent offset in the measured ratio of intensities. Simulations in the specific case of NIO1 were carried on, taking as medium length the diameter of the source ($L = 178mm$) and the range of possibile cesium density between $10^{13}m^{-3}$ and $10^{17}m^{-3}$.

The results obtained with this activity are shown in fig. 3.6. It can be seen that the background offset B determines a sort of saturation, i.e. a flat-top, in the absorption signal. It is evident that the integral of the aborption signal is then reduced, causing an underestimation of the density and a correction should be applied. In fig. 3.7 the relation between the real value of density versus the measured density for different value of offset B is shown: there is no need of correction for the density if the measured value is under $10^{16}m^{-3}$. The correction instead increases rapidly for increasing density and the correction factor, i.e. the ratio between real density and the measured one, is very sensitive to the value of B (fig. 3.8).

The effects resulting from background emission are not so subtle as those due to depopulation, as they are directly identified from the shape of absorption signal presenting the flat-top. Two possibile strategies can be adopted in order to have correct measurements:

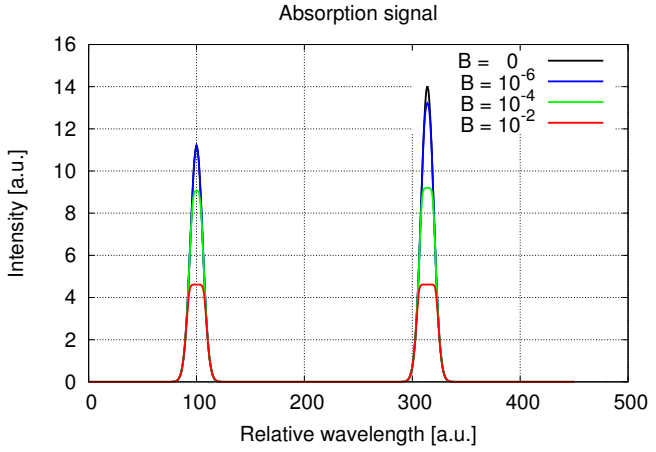

Fig. 3.6: Plot of the absorption signal at different values of offset B.

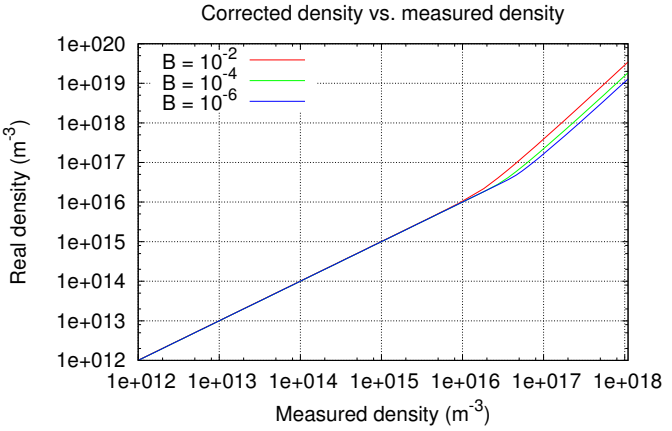

Fig. 3.7: Relation between the real density and the measured density for different values of offset B.

1. the value of the offset B can be directly determined by the height of the flat-top, then used to compute the correction factor from simulations and so the corrected density; this might be difficult if the absorption signal has much noise, because of the sensitivity of the correction factor on the value of B

2. the correct value for the integral of the absorption signal can be calculated by a fit of the peaks discarding the points in the flat top; in case of high offset this strategy can lead to large errors in the fitting procedure and then in the density estimation.

The best strategy to overcome this problem (in case it will turn out to be significant) can be identified only experimentally during the first operations of this diagnostics, once the amount of signal noise and the relevance of the background effects with respect to the signal will be directly observed.

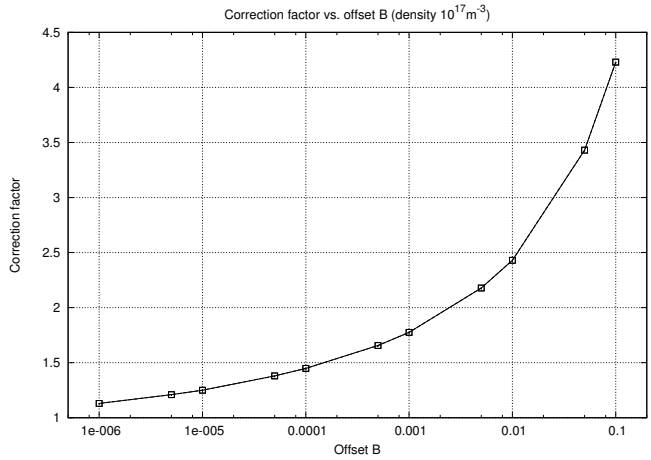

Fig. 3.8: Correction factor for the worst case scenario (i.e. density of $10^{17}m^{-3}$) as a function of offset B.

Chapter 4

Cooling system and calorimeter

4.1 Grid and source cooling system

The plasma source as well as the grids of the acceleration column are actively water cooled. In the source there are five cooling groups: four of these are in the front of the multipole and they consist of seven circuits each, as can be seen in fig 4.1 where two of these groups are represented and water flow is indicated by the numbering; the fifth group is placed in the rear of the multipole, consisting of four circuits as showed in fig 4.2. The difference in temperature between the outlet and inlet flows is evidently related to the power absorbed by the plasma and then deposited to the source walls, and thermocouples are used in order to measure the temperature of the water flowing in the pipes, both for calorimetry purpose and for protection purposes.

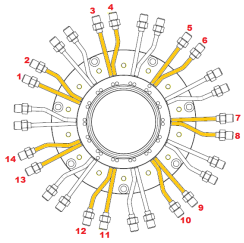

Fig. 4.1: Cooling circuit of the front multipole in the source.

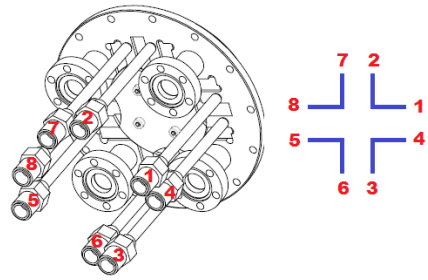

Fig. 4.2: Cooling circuit of the rear multipole

4.1.1 Technical issuses regarding thermocouples

Thermocouples cannot be placed in direct electrical contact with the tubes in the source, which are biased to high voltage, since it might be hazardous for the acquisition system. In fact simulations pointed out that, during breakdowns, oscillations in voltage between the source and the high voltage deck (where all the instrumentation is placed) might arise with amplitude up to several kV. For this reason they have to be attached to a metallic support between two plastic (Rilsan) tubes: in such a way the support can be biased at a fixed desired potential, avoiding the dangerous high voltage oscillations eventually occurring.

Part of the thesis activity dealt with the determination of thermocouple specifications in order to find the most suitable for the purposes and then with the study of different fastening systems, analyzing advantages and disadvantages of every method. The principal parameters that were taken into account for determining the thermocouples type was the temperature range of operation needed and the sensitivity, together with the environment where they are supposed to operate, which is an important consideration especially for the choice of the insulating material.

Considering the specific purposes, the thermocouples types and characteristics chosen were:

- E-type (Chromel-Constantane, butt welded, 0.2mm^2), which has the highest sensitivity and for which the temperatures supposed to be measured during experiment are well inside the operative range (-200°$\div$ 900°). In addition the materials are amagnetic, to prevent any problems that might arise due to magnetic fields.

- Teflon (PFA) isolation (max. working temperature 260°C), since there is no need of using vacuum-comaptible materials

- Twisted wires, to avoid or at least reduce the collection of RF noise which is much near to the position where thermocouples are placed.

- Thermocouples enclosed in a metallic box, in order to achieve two purposes: having a support for the tube and extending the screening also to the ending part of the thermocouples which cannot be sorrounded by their metallic shield.

A particular attention has to be paid to the fastening system: a metallic clamp can be used, since it represents a fast and easy method, but with the disadvantage that thermal inertia of the tubes can delay the measurement, acting as a sort of "low pass filter", i.e. it makes impossibile to observe rapid variation in temperature. For this reason an alternative was studied, which consists in having thermocouples

Type	Temp. Range	Std. Limits of Error
J	0°C to 750°C	Greater of 2.2°C or 0.75%
K	-200°C to 1250°C	Greater of 2.2°C or 0.75%
E	-200°C to 900°C	Greater of 1.7°C or 0.5%
T	-250°C to 350°C	Greater of 1.0°C or 0.75%

Table 4.1: Specifications of different thermocouple types.

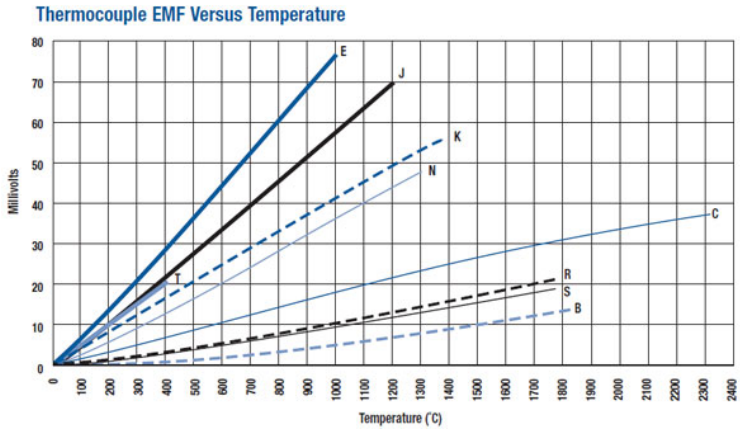

Fig. 4.3: Electromotive force as function of temperatures for different thermocouple types.

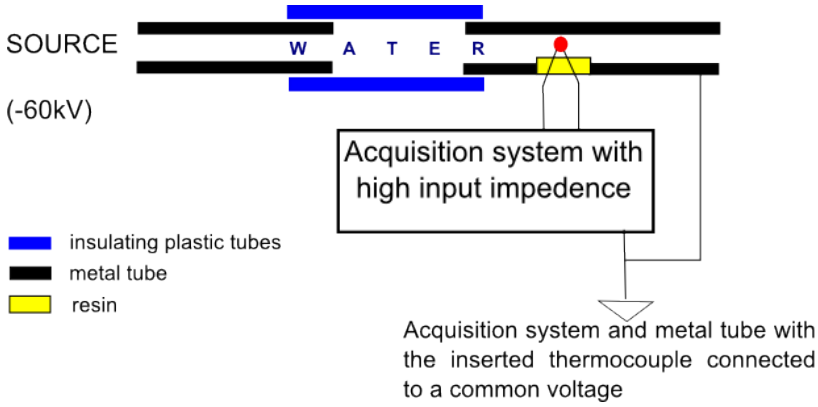

Fig. 4.4: Scheme of the thermocouple mounted in direct contact with the water.

Fig. 4.5: Prototype of the tube with the thermocouple in contact with water.

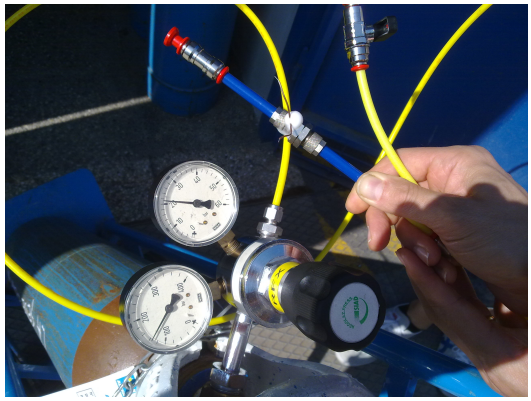

Fig. 4.6: Testing the prototype with helium up to 20 bar.

in direct contact with the water inside the tube. Some prototypes were realized using wires of the same size and isolation material of thermocouples.

The first trial consisted in drilling a hole in a steel barbed fitting tube and inserting the two wires without stripping the insulation. The hole was then sealed with a resin, Araldite 2011, which is water resistant and electrically insulating. In fig. 4.4 a scheme is shown: the metal tube where the termocouples are inserted must be held at the same voltage of the measuring system. In particular the acquisition system must have an high input impedance to avoid curent flowing in it, due to the difference in voltage between the source and the metal tube containing the termocouple. This configuration was tested with helium at high pressure and turned out to be not suitable since resin had not enough adherence to the PFA

coating of the wires, determining leakage at high pressure. So other new prototypes were realized, this time stripping the insulation of the wires so that resin can adhere directly to the metal.

One of this prototype is shown in fig 4.5: it was tested with helium up to a pressure of 20 bar without showing any leakage. Since the maximum pressure of the water in the cooling system is estimated to be around 8 bar, this option is a reasonable alternative that can be used.

The most important issue that has to be considered is that the metallic wires of the thermocouples must not be short-circuited by the metallic connection tube, otherwise a virtual junction is created. As an example in fig. 4.6 was represented what happens if a leakage resistance between the two wires arises. Since the thermocouples wires section is very small, its series resistance R_S will be high, so that $R_L \ll R_S$. In this case the junction appears to be at R_L and the voltage measured will then be proportional to T_1 and not to T_2. Therefore if short circuit between the wires occurs due to a contact between them during the bonding with the reisn or due to a contac with the metallic tube, the temperature measured is that of the tube and not that of the water.

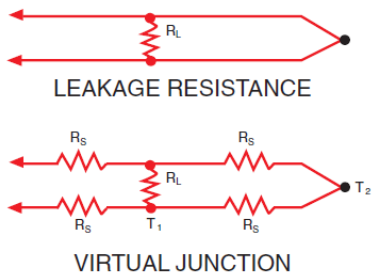

Fig. 4.7: Schematic of a virtual junction due to short-circuit between the wire of thermocouples.

For this reason prototypes were checked using a tester which can measure up to 20MΩ, ensuring the resistance is surely greater than that value, and so no short-circuits occurs, and that Araldite was insulating enough. This work has thus shown that this fastening solution is suitable for the purposes, having passed the aforementioned tests and can then be adopted for all the thermocouples used to measure temperatures in the source cooling system.

The overall advantage of this system is that the precision and the time resolution of the mearurement is increased, but it presents also some disadvantage with respect to clamping the thermocouples directly on the metal tubes: a plastic extension tube is needed and there is the risk (also if it is very unlikely) of small pieces of thermocouples breaking inside the tube and being transported by the water flow.

4.2 Beam calorimeter

The calorimeter is one of the NIO1 beam diagnostics used to determine the intensity profile of the beam. As can be seen in fig. 4.8 and 4.9 , it consists of a copper plate target, acting as beam dump, with thirteen parallel tubes inside. The tubes outside the copper plate has an outer diameter of 6mm and a inner diameter of 5mm, with a spacing between them of $\sim$ 5mm

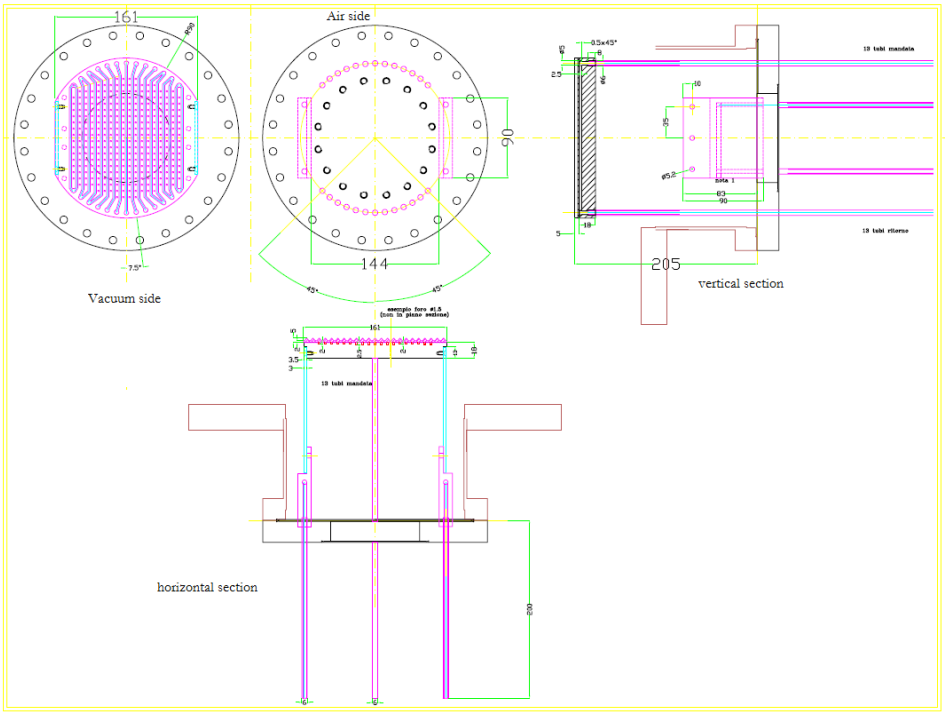

Fig. 4.8: Drawing of the calorimeter designed for NIO1.

The power deposited by the beam determines a difference in temperature between inlet and outlet flows, which can be measured by thermocouples. An estimate of the power can then be computed combining the measurements of the differential temperature ΔT and of the water flow. The relation between the thermal power P_{th} due to the beam impinging the plate and the temperature difference ΔT for a given water flow rate $\dot{m}$ and using c_{H_2O} as the water specific heat:

$$\Delta T = T_{\text{out}} - T_{\text{in}} = \frac{P_{th}}{\dot{m} c_{\text{H}_2\text{O}}} \tag{4.1}$$

A two-dimensional beam intensity profile can be achieved rotating the calorimeter by 90° and reproducing identical operating conditions. To perform this rotation the flange has to be opened, loosing vacuum, and therefore this 2D measurement cannot be done run-time.

The calorimeter is used also to measure the emittance pattern of the beams thanks to pepper-pot method: a square matrix of 1.5mm diameter holes is present in the copper plate so that the beamlet transmitted can be observed from the back by a scintillator and a CCD camera. This instrument allows a measurement of beam emittance pattern faster than an Allison scanner, since there is no need of moving the slit to obtain a scan in position, which is instead achieved thanks to the holes array.

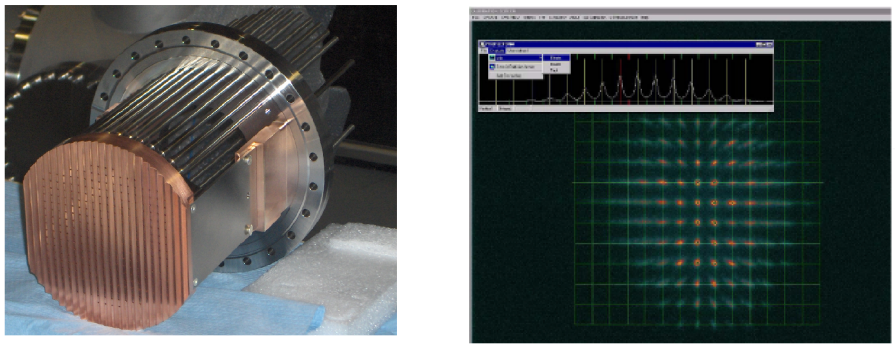

Fig. 4.9: Left: picture of the NIO1 calorimeter. Right: an example of the application of the pepper-pot method.

4.2.1 Thermocouple fastening

The principal difference about the requirements that calorimeter thermocouples have to fulfill with respect to the ones for the source is that the insulating material has to be vacuum compatible and high temperature resistant: for this reason kapton was chosen. The main constraints that have to be considered in dealing with the choice of the fastening method are:

- High temperature (up to 200°C)
- Vacuum compatibility
- Elasticity of fixing material
- Geometry, i.e. limited space between the tubes ($\sim$ 5 mm) and the low outer diameter (6mm).

The first option considered was represented by cable ties usable down to a loop diameter of less than 6mm to ensure enough fastening strength and with a vacuum compatibility material. Steel cable ties should be a good option, but those commerically available do not comply with the pipe diameter requirement. A solution is represented by Polyether Ether Ketone (PEEK), a thermoplastic polymer which is not hygroscopic and it is vacuum compatible. Technical specifications for the cable tie model considered are given in table 4.2 along with the technical drawing and the photo of a specimen.

Material	PEEK
Opererating Temp.	-55°C to 240°C
Max. Bundle diam.	35.0mm
Min. Bundle diam.	4.0mm
Min. Tensile strength	230N
Length (L)	145mm
Width (A)	3.4mm
Thickness (T)	1.2mm
Head heigth (C)	4.5mm
Head length (B)	5.7mm
Head width (D)	6.1mm

Table 4.2: Specification of the PEEK cable ties.

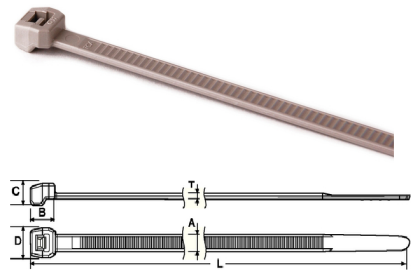

Fig. 4.10: Picture of the cable ties.

The main disadvantage of this solution is that PEEK migth not be resistant enough against ionic bombardment, which might fastly deteriorate the material. In order to avoid this deterioration a protective carter should be studied, but this would complicate much more the system. Hence, the other possibility which fullfills all the requirements about temperature and vacuum enviroment is featured by stainless steel clamp. The problem with this solution is that there are no commercially available clamps which are suitable considering the geometry constraints, i.e. the small diameter and space between tubes, the necessity of having a clamp that can get fully opened. As a consequence they have to be made for the specific purpose, with the same design of the hose clamp shown in fig 4.11.

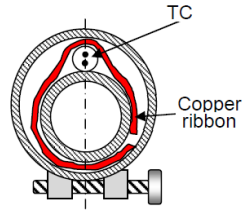

Fig. 4.11: Schematic of the stainless steel clamp for thermocouple fastening.

Chapter 5

Photometry and Spectroscopy

In this chapter, the optical diagnostics with which NIO1 source is provided during the first opertations will be presented and the preliminary activities to set them in operation are explained. The operational diagnostics implemented are:

- Plasma light detection, achieved by a photomultiplier. This diagnostic is useful to detect plasma ignition and for photometry, and to study the dynamic with high time resolution.
- Source emission spectroscopy:
  - low-resolution, wide range (200nm - 800nm) mini-spectrometer
  - high-resolution, Czerny-Turner spectrometer (f = 750mm, slit 70μm, grating 1200g/mm, spectral width $\sim$ 7nm).

5.1 Plasma light detection system

The optical system for plasma light detection consists of a telescope that collects plasma light and focuses it into an optical fiber (diameter of 400μm), which is coupled to a photomultiplier for the detection. The telescope is made up by a cylinder with a lens in one side and a fiber holder in the other side with a sliding screw for focusing; the focal length of the lens is 50mm with a diaphragm diameter of 4mm and the window through which plasma is observed is placed in the rear plate of the source. The photomultiplier module (fig. 5.1 used is an HAMAMATSU (model H10722) which has an integrated high voltage generator and an externally adjustable gain that can be set up thanks to a control voltage in a range between

0.5V and 1.1V. The output signal is a voltage signal achieved by an internal transimpedence amplifier with gain of 1V/μA and bandwith from DC to 20kHz. A power supply was designed and realized in order to provide the voltages needed (i.e. +5V,-5V, GND), with integrated gain control circuit. The scheme of the circuit is showed in fig. 5.2 .

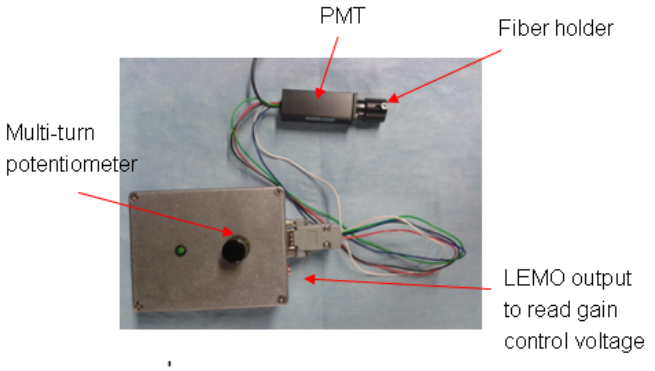

Fig. 5.1: Picture of the photomultiplier and its power supply.

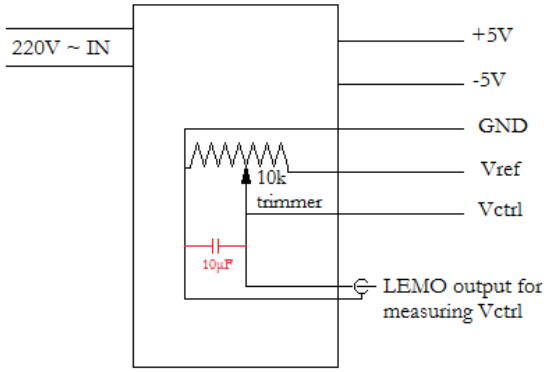

Fig. 5.2: Electric scheme of the PMT power supply. Note in red the capacitor for the stabilization of gain control voltage.

Voltage regulation for gain control is achieved by a 10kΩ multiturn potentiometer, so that voltage can be set with a resolution of $\sim$ 1mV. To check the response of the PMT, it was illuminated with a light of constant intensity and the voltage

output signal was recorded for different values of control voltage. During this operation output signal and control voltage were monitored thanks to an oscilloscope, so that also the RMS of noise was measured.

Vcontrol (V)	Vsignal (V)	Signal Noise ($mV_{pk,pk}$)
0.503	0.146	50
0.520	0.198	50
0.539	0.264	50
0.550	0.316	50
0.575	0.460	50
0.587	0.512	100
0.602	0.602	100
0.655	1.17	200
0.710	2.60	500
0.730	3.34	500

Table 5.1: PMT output signal and noise as a function of gain control voltage with a constant illumination. Data were measured before the insertion of the stabilizing capacitor.

Plotting V_{signal} versus $V_{control}$ (fig. 5.3) the relative gain as a function of the control voltage is obtained. If a constant light signal is acquired, the output voltage depends on the control voltage according to the function:

$$\ln(V_{output}) = A \cdot \ln(V_{ctrl}) + B \tag{5.1}$$

where the constants calculated are $A = (8.2 \pm 0.1)$ and $B = (3.74 \pm 0.08)$.

It can be easily seen from the data in table 5.1 that the level of peak to peak noise strongly increases with incresing control voltage, reaching the 20% of the mean output voltage. Observing the signals in the oscilloscope it was evident that the control voltage was strongly affected by noise too. This noise seems to have an high-frequency component of $\sim$ 6MHz and a low-frequency component of $\sim$ 250kHz. Therefore the cause of the output signal noise can be due to these instabilities of control voltage, which have an amplitude peak to peak of $\sim$ 10mV and to test this hypothesis the oscilation in output voltage due to the noise in control circuit, eq. 5.2 is used:

$$\delta V_{out} = \exp(A \cdot \ln(V_{ctrl} + \delta V_{ctrl}/2) + B) - \exp(A \cdot \ln(V_{ctrl} - \delta V_{ctrl}/2) + B) \tag{5.2}$$

where δV_{out} is the peak to peak amplitude of the noise in output signal due to the noise in control voltage of peak to peak amplitude δV_{ctrl}. Using $\delta V_{ctrl} \sim 5mV$, in fig. 5.4 the noise measured and the noise calculated by eq. 5.2 versus the control voltage are plotted.

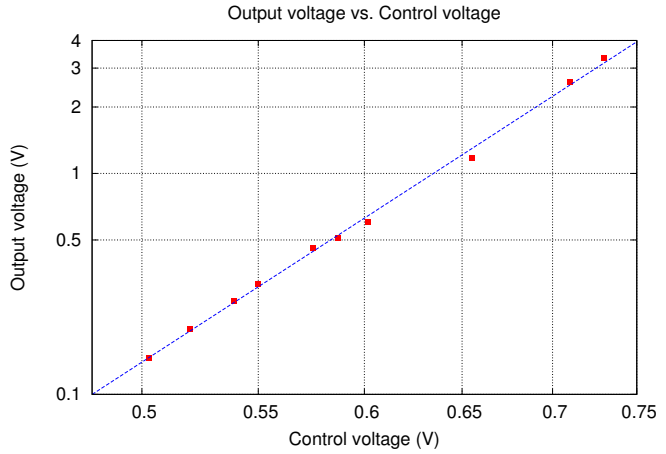

Fig. 5.3: PMT of the output voltage as function of gain control voltage for a constant illumination. In red the experimental points and in blue the fitting curve. The plot is in logarithmic scale.

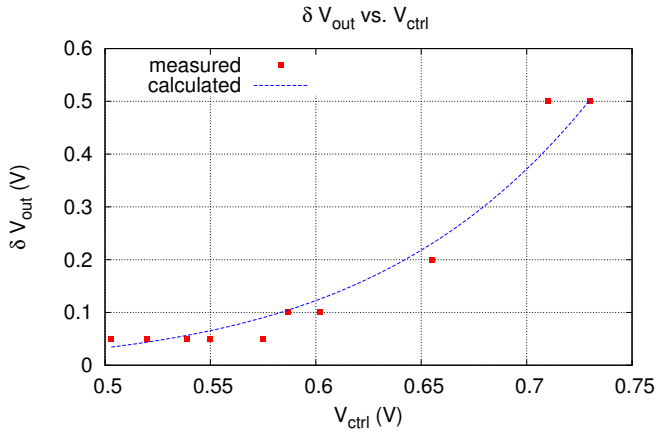

Fig. 5.4: Peak to peak noise of the output signal plotted as a function of the gain control voltage. In red the experimental measurements and in blue the calculated noise from eq. 5.2.

The noise level is quite compatible with the estimate of eq. 5.2, and it is then possible to conclude that much of the noise in the output voltage is caused by the

gain control instability. To improve the stability of the control circuit a capacitor was inserted in parallel to the potentiometer for control voltage adjustment, as shown in red in fig. 5.2. In such a way a greater level of stability was achieved determining also a better signal to noise ratio for the output voltage. The new measurements after the introduction of the capacitor are reported in table 5.2.

Vcontrol (V)	Vsignal (V)	Signal Noise ($mV_{pk,pk}$)
0.501	0.163	15
0.522	0.233	15
0.540	0.318	15
0.550	0.359	15
0.580	0.574	30
0.592	0.600	30
0.600	0.770	50
0.652	1.41	50
0.700	2.51	100
0.733	3.78	100

Table 5.2: PMT output signal and noise as a function of gain control voltage with a constant illumination. Data were measured after the insertion of the stabilizing capacitor.

5.2 Source emission spectroscopy

For the source emission spectroscopy the lines of sight parallel to the plasma grid were used, one for the wide-range, low resolution spectrometer, and the other one for the high resolution, Czerny-Turner spectrometer. The sketch in fig. 5.5 shows the telescopes used to collect light, in which 50mm focal length lenses and 4mm diameter diaphfragm were used, the same as for the photomultiplier.

In this part of the thesis work the optical systems was assembled and mounted on the source and focused back-illuminating the fibers. Attention was paid not to introduce vignetting, so that also absolute intensity measurements can be carried on with this experimental setup. During these operations an important weakness point regarding the fiber holder was discovered: as a matter of fact some of the fibers were broken exactly on the clamping point, and they had to be repaired by cutting and polishing, a very delicate and time consuming task. For this reason in the future a better fiber holder solution will be devised, with a design compatible with connectorized and armored optical fibers.

In order to obtain absolute intensity measurements the optical system was calibrated using an Ulbricht integrating sphere with a 10W lamp. The emission spectral intensity of the lamp is known and is plotted as a function of wavelength.

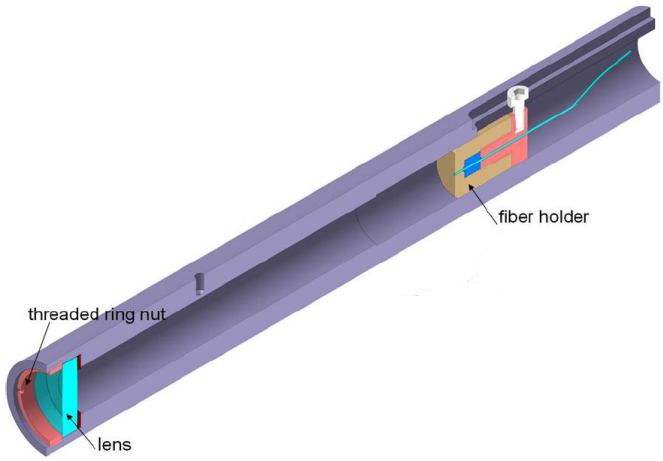

Fig. 5.5: Sketch of a telescope used to collect and focuse ligth in an optical fiber for source emission spectroscopy.

Some spectra of the lamp at different integration times were taken, so that the conversion factor between counts per seconds given by the CCD and the absolute intensity (i.e. photons per unit area per unit time) can be computed and the CCD linearity response checked. Let $S(\lambda)$ be the signal recorded by the CCD at an integration time equal to ΔT, $B(\lambda)$ the background measured at the same integration time and $I(\lambda)$ the spectral intensity of the lamp as in fig. 5.6, then the conversion factor is given by:

$$k(\lambda) = \frac{\frac{I(\lambda) \cdot \lambda}{hc}}{\frac{S(\lambda) - B(\lambda)}{\Delta T}} \tag{5.3}$$

where the multiplication $I(\lambda) \cdot \frac{\lambda}{hc}$ is used to convert power into number of photons per second. Therefore the wavelength dependent calibration factor can be multiplied by the time-normalized spectrum, in order to achieve absolute intensity measurements. An example of the normalized spectrum of the lamp and the calibration factor k is represented in fig. 5.8.

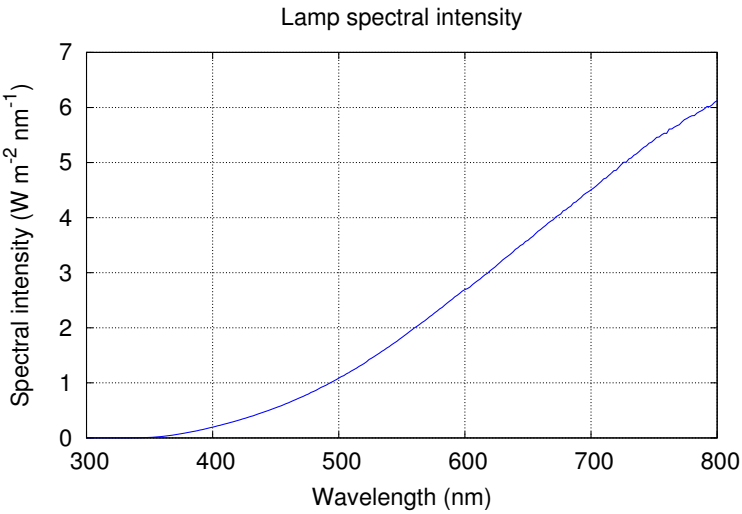

Fig. 5.6: Spectral intensity curve of the lamp used for calibration of optical emission spectroscopy system.

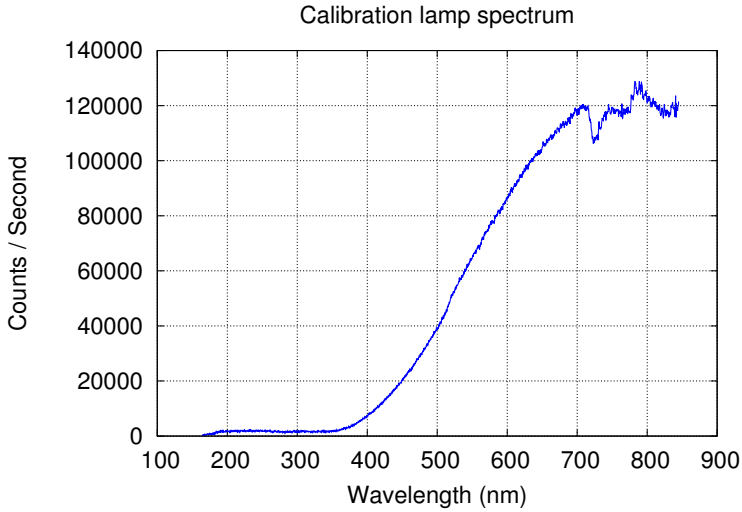

Fig. 5.7: Normalized spectrum of the calibration lamp obtained by the low resolution spectrometer.

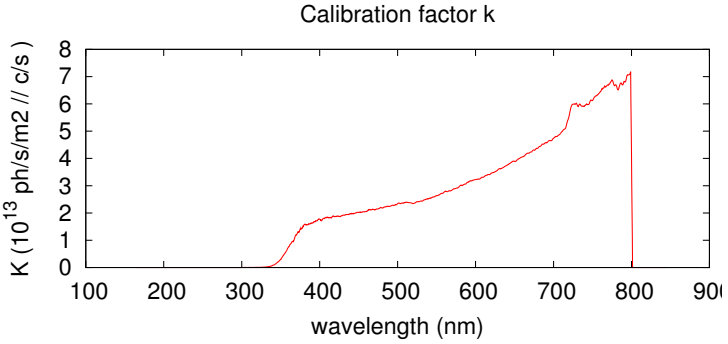

Fig. 5.8: Calibration factor as a function of wavelength. By multiplying the measured spectra by this factor, a absolute intensity spectrum is obtained.

The other important issue is the linearity response of the CCD detector of the spectrometer: in order to verify this response, spectra of the lamp at different integration times were measured, as well as the background signals. In fig. 5.9 the number of counts for different values of integration time at a fixed wavelength is plotted together with the line resulting from the fit of the three points at low integration time (i.e. low counts), which gives the expected counts if linearity is preserved. The entity of this saturation can be measured by the parameter:

$$S = \frac{n_{counts} - n^{\star}_{counts}}{n^{\star}_{counts}} \tag{5.4}$$

where n_{counts} is the expected number of counts in case of a perfect linear response and $n^{\star}_{counts}$ is the effectively measured number of counts. The expected counts are computed by a proportion from the data at low integration, i.e. $n_{counts}(\Delta t) = n_{counts}(\Delta t_0)\frac{\Delta t}{\Delta t_0}$. In the plot of fig. 5.10 is represented the correction factor S as a function of the measured number of counts and in such a way it is possible to calculate the correct number of counts. Considering that the maximum counts number is 64000 and that it is preferable to avoid going over 32000 counts, the maximum error due to the nonlinearity is around 7%.

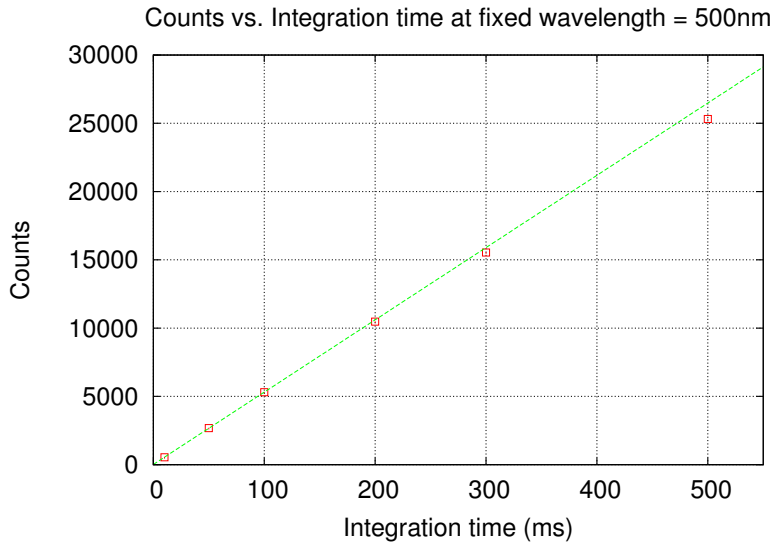

Fig. 5.9: Number of counts vs. integration time for a fixed wavelength

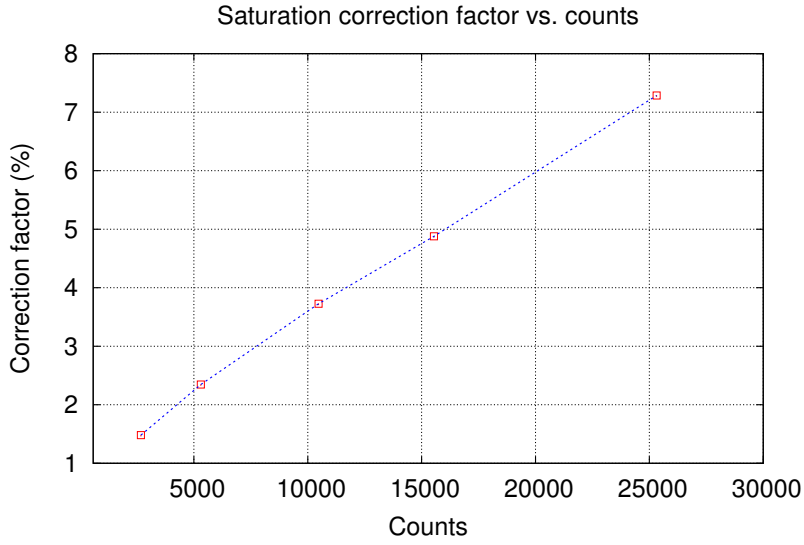

Fig. 5.10: Correction factor defined in eq. 5.4 in order to take into account saturation.

Chapter 6

First NIO1 operation in air

During the present thesis work, the NIO1 RF source was turned on for the first time. The first operations of NIO1 experiment involved the plasma ignition of the RF source without acceleration and the acquisition of data by the optical diagnostics, i.e. source emission spectroscopy and plasma light detection, in order to assist the initial operations and have an estimate of plasma parameters (such as electron temperature). During these operations some tests were carried out in order to find the best coupling (impedence matching) between the RF power supply and the plasma. Atmospheric air was used as filling gas, instead of hydrogen. The reason of this choice is that, once acceleration will be turned on, in order to obtain a hydrogen beam of acceptable intensity, it is necessary to evaporate cesium in the chamber. Since cesium oven will be available only later on in the future, using air it is possible to achieve a more intense beam of accelerated negative oxygen ions, thanks to their electronegativity. In such a way an acceptable intensity for the beam could be achieved, so that the extraction and acceleration system can be tested before the Cs oven will be available. The discharge parameters that can be controlled by the experimental setup that will be discussed in detail in the next setion are frequency of RF, forward power and pressure. In order to understand the dependence on these parameters of the dicharge characteristics, the following measurements were carried out:

- Frequency scan to find the best matching with RF power supply
- Power scan up to 300W at fixed pressure
- Pressure scan (0.1Pa ÷ 12Pa) at fixed power

6.1 Experimental setup

The sketch in fig. 6.1 shows the layout of the experimental apparatus used in this campaign. The pressure is set by regulating the flow through a voltage controlled valve. The RF power supply is controlled through a serial port by a LabView interface, so that it is possible to set the frequency and the RF forward power as well as to read the reflected power (i.e. reflected by the plasma and by the RF line).

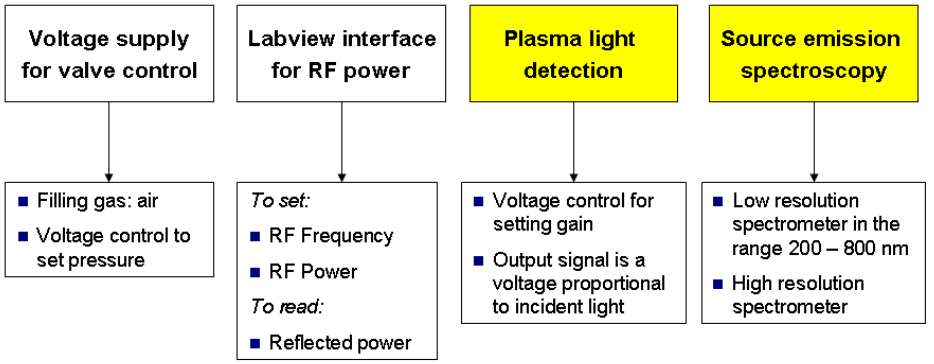

Fig. 6.1: Sketch of the layout of the experimental apparatus to control the RF power and the diagnostics.

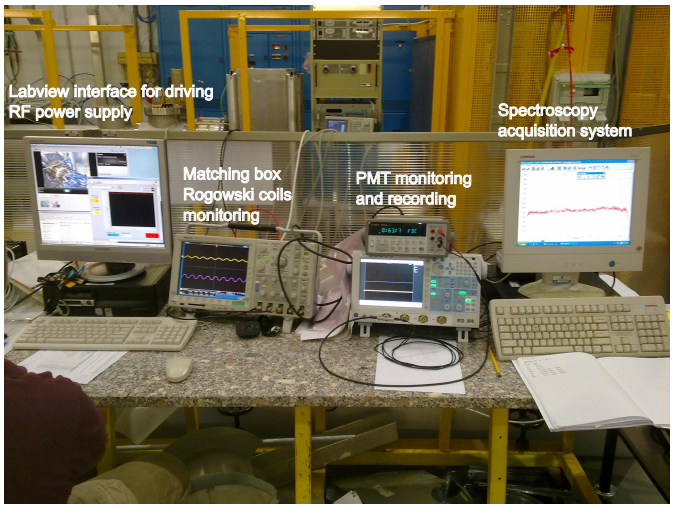

Fig. 6.2: Picture of the experimental setup.

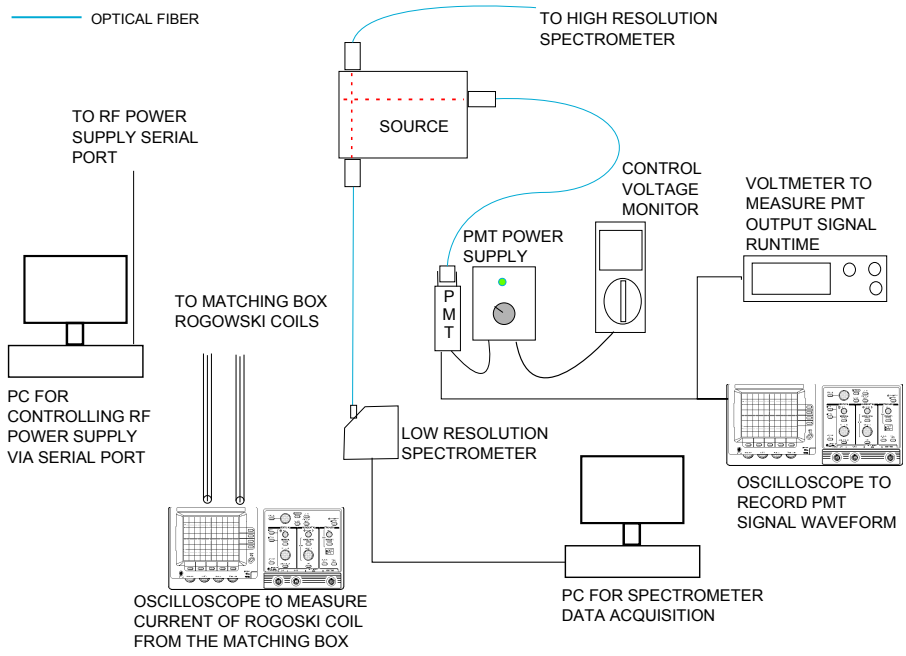

Fig. 6.3: Schematic of the experimental setup used for first NIO1 operation. Note the two diagnostic system used, i.e. emission spectroscopy and photometry.

6.2 Measurements and results

Measurements were taken by varying the value of forward power, while mantaining the pressure fixed, so that three power scan was obtained for pressure value sof 1.1Pa, 6Pa and 10.5Pa. The pressure scan between 0.1Pa and 10Pa was carried out at a constant power of 170W. For every discharge condition plasma light as well as low and high resolution emission spectra were recorded. In the following the results will be presented together with a description of the analysis methods.

6.2.1 Plasma light

The signal of the photomultplier was recorded by an oscilloscope so that it could be easily observed during the operation and signal waveform recorded. As described in section 5.1 the voltage output of the photomultiplier is a measure of plasma light intensity and with this diagnostic it is possibile to identify plasma ignition or disruption. In fig. 6.4 the PMT signal of the very first operation of NIO1 is

shown, in which the output voltage is plotted versus time. It is possible to observe the ignition of the plasma with the minimum power of 30W at t $\sim$ 55s and then the step increments of power up to 60 W.

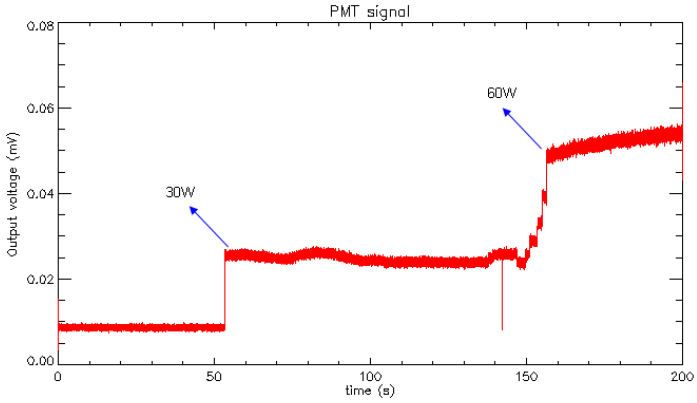

Fig. 6.4: Photomultiplier signal for the first run of NIO1. It can be noted the different value of PMT signal proportional to plasma light for different value of RF power.

The results of the pressure scan at fixed power and of the RF power scan at fixed pressure are presented respectively in fig. 6.5 and 6.6. It can be seen that by increasing pressure the signal of the PMT increases till it reaches a sort of saturation for high pressure value. This can be explained by considering that at very low pressure the mean free path of electrons is very large and so there are fewer collisions, which are responsible for ionization and excitation and then light emission. If the mean free path is reduced (i.e. pressure increased), collisions are enhanced and so are excitation and light emission. For high value of pressure anyway, the energy acquired by electrons is gradually reduced because of the very short mean free path, and so is excitation and then light emission which slowly decreases. The maximum light emission appears to be in the pressure region between 4Pa and 6Pa.

The results of power scan at different pressures can be observed in the plot of fig. 6.6, which shows an increase of the light emission with increasing power. In particular it is evident there are two different regimes: at low power (under 120W) plasma light intensity increases exponentially, as shown in fig. 6.7; for values of power above 120 W the plasma light intensity shows a linear dependence with respect to power (fig. 6.8). These two different trends for different values of power have to be better invenstigate in the future, for example using the line of sight next to plasma grid. In such a way it will be possible to understand if the observed trends are due to a change in shape or position of the plasma. It can be easily observed that the trend noted earlier with the pressure scan is respected, i.e.

the plasma light values for the power scan at 1.1 Pa are always much lower than those measured at 6Pa and 10.5Pa and that the maximum plasma light values were recorded at 6Pa pressure.

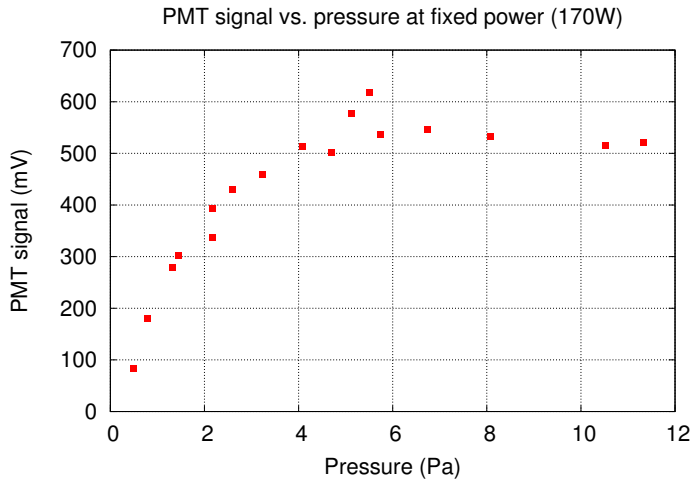

Fig. 6.5: Pressure scan of the PMT signal acquired at fixed power of 170W

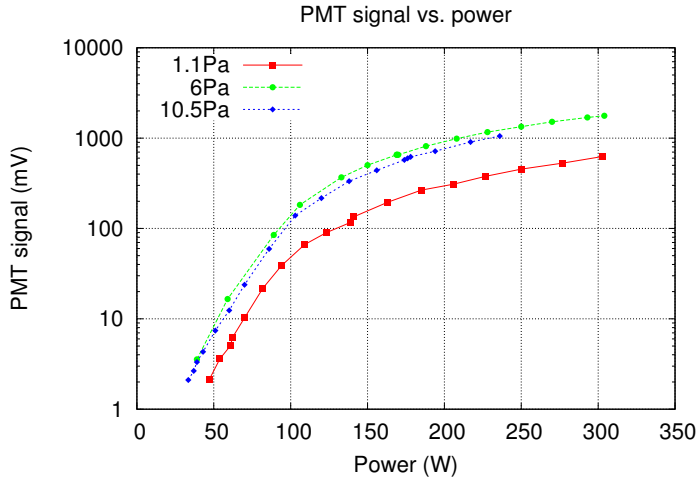

Fig. 6.6: PMT signal vs. RF power, in three different pressure conditions: 1.1Pa, 6Pa, 12Pa.

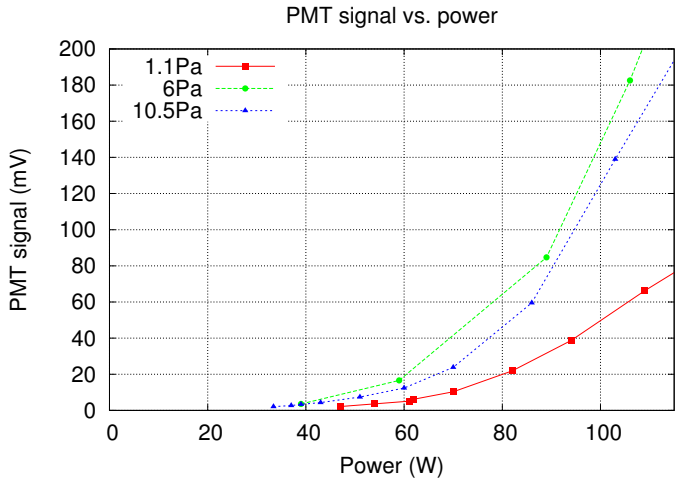

Fig. 6.7: Detailed view of the PMT signal power scan in the low power region. Note the exponential increasing of plasma light intensity.

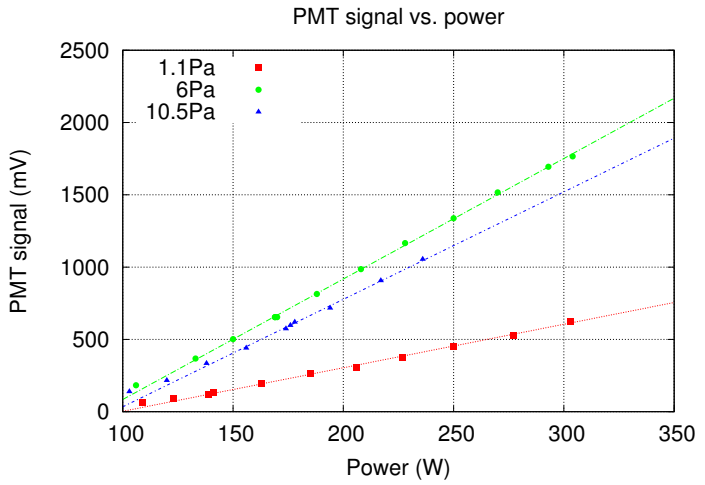

Fig. 6.8: Detailed view of the PMT signal power scan at high pressure. Note the linear dependence of light intensity on power.

6.2.2 Spectroscopy

Air is mostly composed by nitrogen, and therefore, considering the cross sections in the observed spectral region, the spectrum is dominated by molecular nitrogen emission, as can be seen in fig. 6.9, where the bands of the first positive system and the second positive system of nitrogen molecule can be observed [32].

These are transitions between different electronic state of the neutral N_2 molecule: since nitrogen is a biatomic molecule in the spectrum the transition between different electronic states appears as roto-vibrational bands, i.e. transition between states with different vibrational and rotational quantum numbers. Also the transitions of the ionized molecule N_2^+ at 391.4nm and 423.6nm can be observed. In fig. 6.10 a detail of the second positive system is shown.

The nitrogen molecule rotational bands is resolvable only with the high resolution spectrometer, with which also the triplet of atomic oxygen at 777nm was resolved. No evidence of other species was observed.

The first analysis that was performed on those data was oriented to determine the electron temperature as well as neutral temperature. In this type of discharge, the obtained plasma is out of equilibrium, in fact the neutral temperature (i.e. gas temperature) is well below that of electrons. Since nitrogen is a molecular gas, in addition to electron and neutral temperatures also vibrational and rotational temperatures have to be taken into account, which are related respectively to ion temperature and to gas molecule temperature.

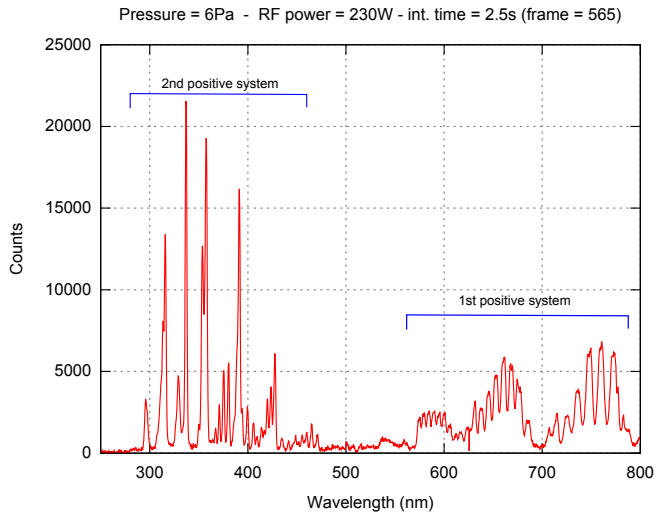

Fig. 6.9: Spectrum measured by low resolution spectrometer.

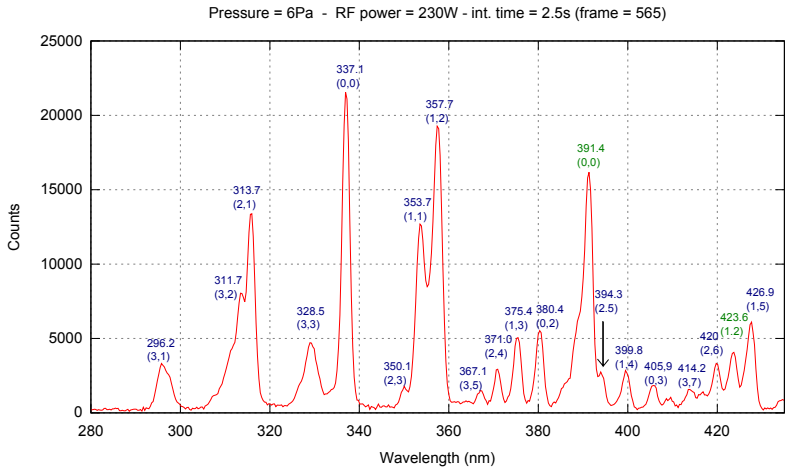

Fig. 6.10: Detailed view of the nitrogen second positive system (peak indicated in blue). In brackets the vibrational levels of the transitions. The peak indicated in green are relative to the transition of the ionized molecule N_2^+.

6.2.3 Electron temperature

The method that migth be used to obtain an estimate for electron temperature is based on the measurement of the line ratio betwenn $N_2^+(B^2\Sigma_u^+,0 - X^2\Sigma_g^+,0)$ transition at 391.4nm and $N_2(C^3\Pi_u,2 - B^3\Pi_g,5)$ transition at 394.3nm, using the relation between the line ratio and the electron temperature presented in [33] and reported here in fig. 6.11. The plot is based on corona model and in order to be valid the following conditions have to be fulfilled:

- The electron energy distribution function has to be Maxwellian
- The radiative states are directly excited by electron collisions from the N_2 ground state.

The peaks at 391.4nm and 394.3 nm obtained from both high resolution and low resolution spectrometer were fitted with a double gaussian, so that the line ratio can be calculated and then the temperature inferred from fig. 6.11.

Fig. 6.12 and 6.13 shows the estimated value for the electron temperature obtained by the aforementioned line ratio. These results have to be very critically interpreted: they have been measured and obtained for the very first operation of NIO1 and for the first time analysed using the model described above. It is evident that the value obtained by the high resolution spectrometer are systematically higher than those obtained by the low resolution spectrometer.

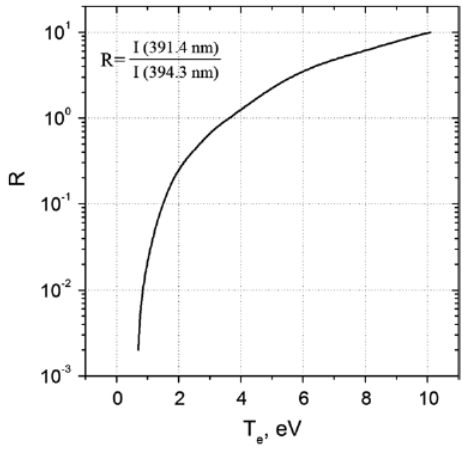

Fig. 6.11: Ratio between 391.4nm and 394.3nm lines plotted as a function of electron temperature [33].

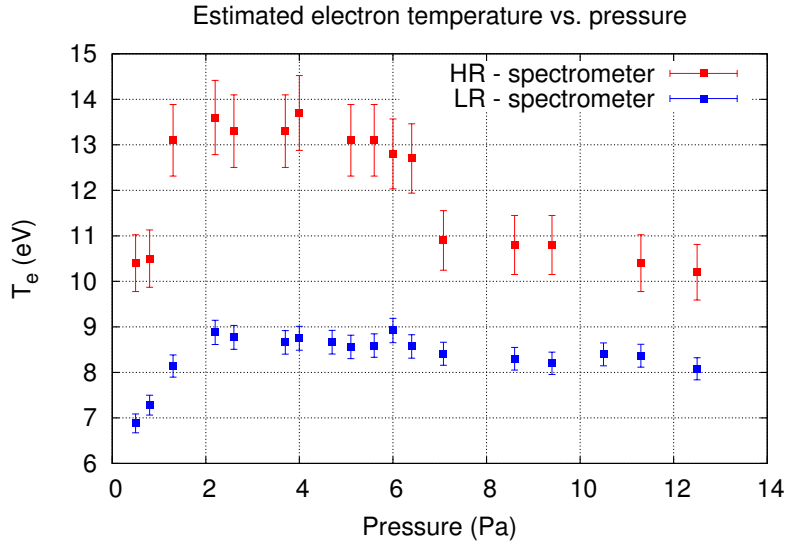

Fig. 6.12: Estimated electron temperature as a function of pressure, calculated using the ratio between 391.4nm and 394.3nm nitrogen lines. In red the data of the high resolution spectrometer and in blue the low resolution spectrometer.

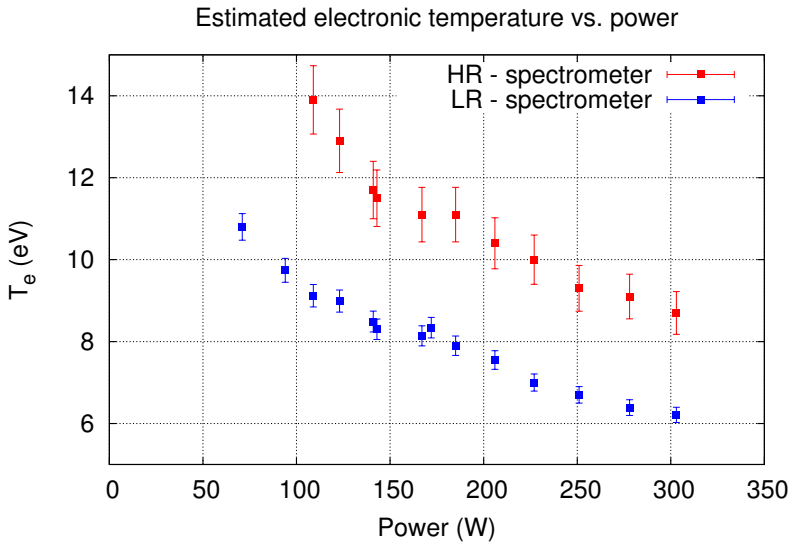

Fig. 6.13: Estimated electron temperature as a function of power, obtained by the line ratio between 391.4nm and 394.3nm nitrogen lines. In red the data of the high resolution spectrometer and in blue the low resolution spectrometer. Note the decreasing trend of estimated temperature with power: this suggests that te model used to analyse these data should be probably rejected.

The reason is that with the low resolution spectrometer the band head transition $N_2(C^3\Pi_u,2 - B^3\Pi_g,5)$ is not resolved from the other vibrational transitions $N_2(C^3\Pi_u,^{v'} - B^3\Pi_g, v^{''})$, which are strongly weaker than the band head but which involve an offset in the determination of the peak value for the line at 394.3nm. Therefore the value of this peak is overestimated and the line ratio is lower than that calculated with the high resolution spectrometer. In the pressure scan at fixed power the estimated temperature seems to increase rapidly with increasing pressure in the low pressure region, reaching a flat top and then slowly decreasing at higher pressure.

It is interesting to observe that the estimated temeperature seems to decrease as power increases. This probabily suggest that the value obtained for electron temperature cannot be considered correct and the model used is inadequate to the specific situation. In particular the hypothesis which is probably not satisfied is the equilibrium state, i.e. the electron energy distribution function might be non-Maxwellian and the plasma is out of equilibrium. This consideration suggests that another, more refined, model should be used in order to correctly evaluate electron

temperature. The proper model to be used could be a collisional radiative model with nitrogen molecules, which is much more complex since it takes into account that the ionization process is due to electron collisions from any bound level and is partially balanced by three-body recombination into any level.

6.2.4 Rotational temperature

For the determination of rotational temperature the rotational band of (0-2) transition was simulated for different T_{rot} and overimposed on the resolved spectrum measured by the high resolution sepctrometry, so that the T_{rot} at which there is the best match between experiments and simulations can be obtained[34]. In order to do this for each value of temperature simulated the deviation with respect to the experimental data were calculated and the temperature is determined as the minimum value of the deviation curve. Let S_0 be the minimum value of the deviations: a confidence interval for temperature estimate is obtained considering the value of T satisfing the condition $S(T) \leq S_0 + \alpha \cdot S_0$. The value choosen for α was 5%, considering that in such a way the inter In fig. 6.14 an example of the comparison between measured spectra and simulation is presented.

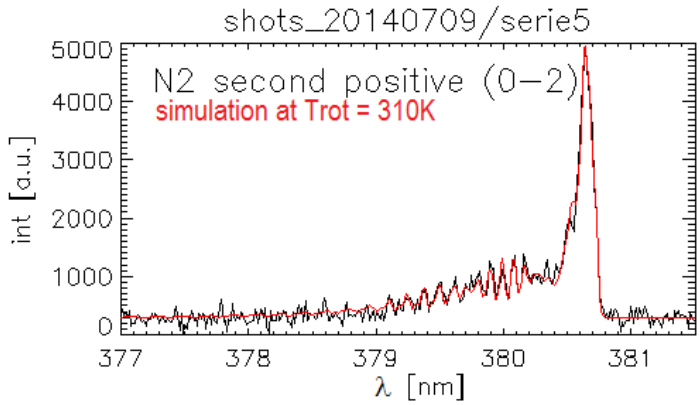

Fig. 6.14: Rotational band of nitrogen spectrum: in black the measured spectrum and in red the simulation.

The rotational temperature as a function of power is plotted in fig. 6.15. With this work it was found that an increase in RF power causes an increase in rotational temperature, which is related to the neutral temperature (i.e. gas temperatures). This is an index of the fact the more kinetik energy is transferred to neutral particles as RF power is raised, and this might be due to an increase in the frequency of ion-neutral collision due to an increase of plasma density.

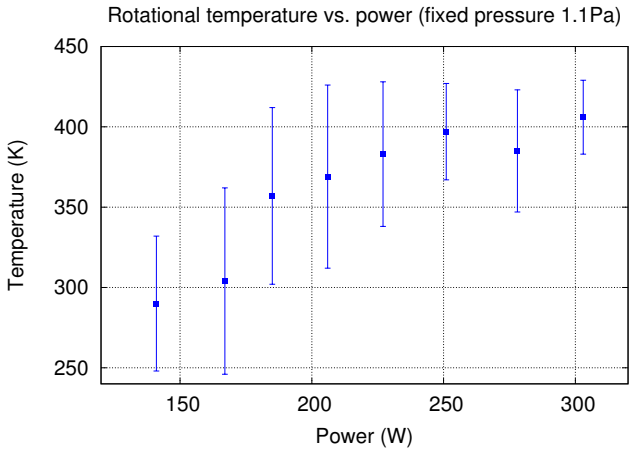

Fig. 6.15: Rotational temperature vs. power at fixed pressure of 1.1Pa.

6.2.5 Vibrational temperature

As for vibrational temperature, it was determined thanks to the second positive system emission spectrum, i.e. considering the transition between the $(C^3\Pi_u, v')$ and $(B^3\Pi_g, v'')$ states which will be denoted in the following as (v',v"): in particular the transition (0-2), (1-3), (2-4), (3-5) were considered.

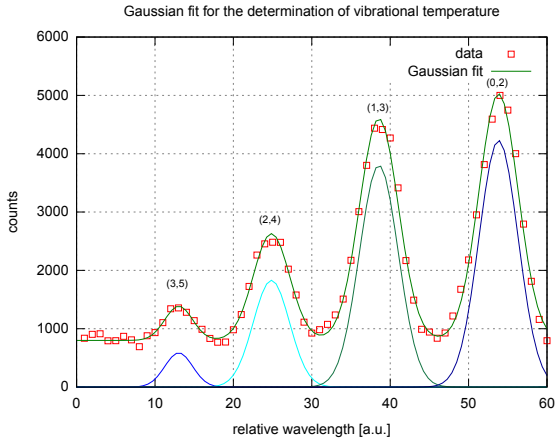

Fig. 6.16: Four Gaussians fit of the vibrational band of the transition $(C^3\Pi_u, v')$ and $(B^3\Pi_g, v'')$.

The procedure presented in [33] was followed: after a normalization of the intensities to the (0-2) transition intensity, the logarithm was plotted as a function of v'. The slope of straight line obtained is related to the vibration temperature by equation 6.1:

$$T_v|_K = \frac{10^4}{3.57 \cdot S - 0.03} \tag{6.1}$$

In fig. 6.18 and fig. 6.19 the ground state measured vibrational temperature are plotted as function of the pressure and the power respectively. Vibrational temperature increases with increasing pressure, reaching the maximum value for a pressure between 2Pa and 3Pa. At higher pressure the temperature then decreases. Looking at the plot in fig. 6.19 it can be observed that vibrational temperature increases with increasing power, more rapidly for low value of power.

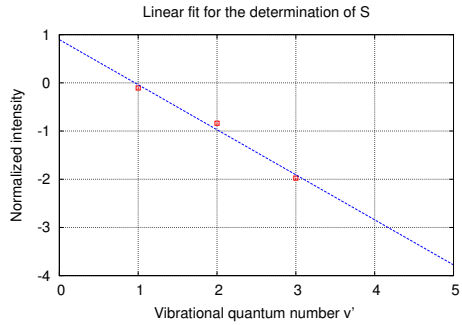

Fig. 6.17: Linear fit for the determiantion of the S parameter and therefore of vibrational temperature by eq. 6.1.

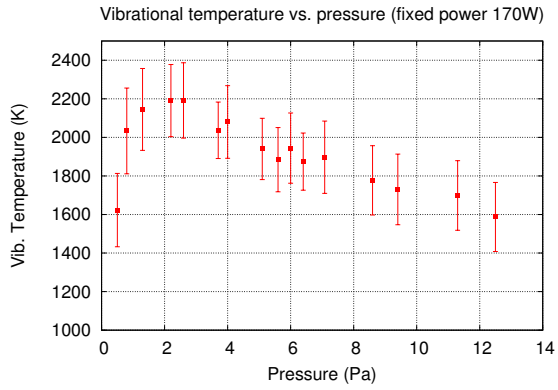

Fig. 6.18: Vibrational temperature vs. pressure at fixed pressure of 170W.

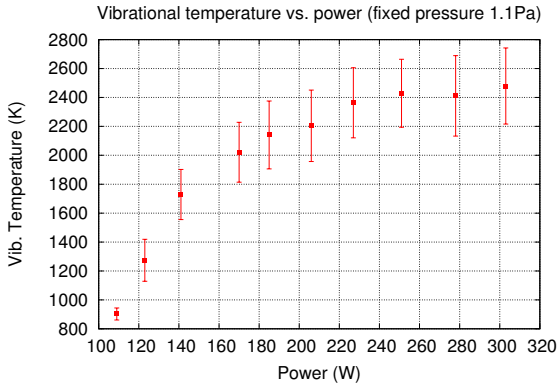

Fig. 6.19: Vibrational temperature as a function of RF power for a pressure of 1.1Pa.

The results presented in this chapter was obtained by the very first data collected by NIO1 experiment. Thus they required much effort, in order to understand the proper way of setting up the diagnostic system and to develop the numerical tools for data management and analysis. Now that most of the preliminary work is done, future experimental campaings can be more focused on obtaining data in the most interesting discharge conditions, to search answers to the open questions, such as that of electronic tempertures, and to give a more consistent interpretation of the data collected.

Chapter 7

Conclusions

This thesis activity allowed to develop and to start the operation of the first diagnostic systems with which NIO1 experiment is now provided, i.e. the optical emission spectroscopy and the plasma light measurement, as well as to propose and test different options regarding thermocouple positioning and fastening for source and beam calorimetry. These solutions has now to be realized and tested during operation, so as to assess which option turns out to be the most suitable. A weakness point of the optical systems was pointed out during the preliminary tests dealing with the optical fiber clamping systems. Due to the small diameter of the optical fiber used (200μm), they have frequently been broken inside the fiber holder.

Furthermore, the design of the laser absorption spectroscopy, a fundamental diagnostic for measuring cesium density once the experiment will be equipped with cesium oven, was developed and denfined in details, identifying its advantages and limits and proposing corrective actions to overcome these limits. Hence the future work will deal with an experimental test to check if the proposed parameters for the optical and electronical systems are suitable for the purposes.

An important goal was achieved: starting the operation of the NIO1 experiment, which is the first negative ion source in operation at Consorzio RFX (Padova), the source was tested and data of the very first plasma were collected. Much effort was required also to prepare the data acquisition system and the numerical analysis tools. The first results of emission spectrocopy have pointed out that it is necessary to collect more data also using other lines of sight, especially the ones on the rear cover, in direction of the source axis. In such a way it will be possible to understand if the trends in temperatures might be due to the fact that plasma shape and position change in the source, or instead if more sophisticated interpretative models must be applied.

Therefore a lot of work has yet to be done, but the results and the observations

collected during this first experimental campaign have helped to identify issues and problems and to define the direction for the future experiments. The implementation of the source and the beam calorimetry, as well as the installation of the laser aborption spectroscopy system, will provide new data in order to clarify these interesting open questions.

References

[1] M. Shimada et al., *"Chapter 1: Overview and Summary."*, Nuclear Fusion 47.6 (2007)
[2] ITER official website, www.iter.org
[3] M. Kikuchi, K. Lackner, M.Tran, *International Atomic Energy Agency*, Vienna (2012).
[4] M. Kuriyama et al., *Fusion Eng. Des.* **39-40**, 115-121 (1998)
[5] ITER Physics Basis Editors et al., *Nucl. Fusion* **39**, 2495 (1999).
[6] R. S. Hemsworth, T. Inoue, *IEEE Trans. Plasma Sci.* **33**, 1799 (2005)
[7] M. Bacal et al., *Rev. Sci. Instrum.* **67**, (1996) 1138
[8] M. Bacal,*Nucl. Fusion* **46** (2006) S250
[9] M. Bacal, *Rev. Sci. Instrum.* **79** (2008) 02A516
[10] M. Bacal, G. W. Hamilton, *Phys. Rev. Lett.* **42** (1979) 1538
[11] Yu. I. Belchenko, G. I. Dimov, V. G. Dudnikov, *Nucl. Fusion* **14** (1974) 113
[12] I. G. Brown, "14. Negative Ion Sources." *The Physics and Technology of Ion Sources*. New York: Wiley, 1989.
[13] M. Cavenago et al. *AIP Conf. Proc.* **1097**, 149 (2009)
[14] M. Cavenago et al. *Rev. Sci. Instrum.* **81**, 02A713 (2010)
[15] M. Cavenago et al., *AIP Conf. Proc.* **1390**, 640 (2011)
[16] M. Cavenago et al., *AIP Conf. Proc.* **1515**, 157 (2013)
[17] U. Fantz, D. Wünderlich,*New J. Phys.* **8**, 301 (2006)
[18] U. Fantz, *Contrib. Plasma Phys.* **44**, 508 (2004)
[19] U. Fantz and B. Herger, Plasma Phys. Control. Fusion **40**, 2023-2032 (1998)
[20] M. Bacal, *Rev. Sci.* **71**, 3981 (2000)
[21] R. Pasqualotto, A. Alfier, L. Lotto, *Rew. Sci. Instrum.* **81**, 10D710 (2010)
[22] C. F. Barnett et al., *Atomic Data for Controlled Fusion Research* ORNL-5206 (1977)
[23] P. Strehl, *Beam Instrumentation and Diagnostics*, XVII, Berlin Heidelberg: Springer, 2006
[24] U. Fantz, *Nucl. Fus. 46*, S297 (2006)
[25] M. Barbisan, *Rev. Sci. Instrum.* **85**, 02A708 (2010)
[26] G. Serianni et al., *Rev. Sci. Intrum.* **85**, 02A736 (2014)

[27] A. Rizzolo et al., *Fus. Eng. Des.* **85**, 2268 (2010)
[28] G. Serianni et al., *"Negative Ion Beam Characterisation in BATMAN by mini-STRIKE: Improved Design and New Measurements"*, presented at Negative Ion Beams adn Sources conference 2014.
[29] U. Fantz, C. Wimmer, *J. Phys. D: Appl. Phys.* **44**, 335202 (2011)
[30] S. Briefi, C. Wimmer, U. Fantz, *Phys. Plasmas* **19**, 053501 (2012)
[31] Demtröder, W. "Chapter 3. Widths and Profiles of Spectral Lines", *Laser Spectroscopy Volume 1: Basic Principles*, Berlin: Springer, 2008.
[32] Herzberg, *Molecular Spectra and Molecular Structure I: Spectra of Diatomic Molecules*, New York: Van Nostrand, 1950
[33] N. Britun et al.,*J. Phys. D: Appl. Phys.* **40**,1022-1029 (2007)
[34] G. Hartmann, P. C. Johnson, *J. Phys. B: Atom. Molec. Phys.*, Vol. **11**, No. 9, (1978), 1597-1612

Ringraziamenti

Numerose sono le persone che in molti modi mi sono stati d'aiuto durante questo percorso, contribuendo alla buona riuscita del presente lavoro, e che per questo sento il dovere di ringraziare. Innanzitutto ringrazio il Dr. Gianluigi Serianni, per la disponibilità che mi ha dimostrato, la passione e la dedizione che mette nel suo lavoro; il Dr. Roberto Pasqualotto, sempre pronto a fornirmi consigli tecnici e non solo, nonché a discutere con me le decine di idee e proposte maturate in questa tesi; il Dr. Marco Cavenago, con cui ho avuto il piacere di collaborare durante le attività sperimentali, condividendo l'emozione della prima accensione della sorgente.

Necessario risulta poi il ringraziamento a Marco Barbisan, dottorando presso RFX, che da subito mi ha aiutato ad ambientarmi ed Ã¨ sempre stato disponibile. Come non dire un grandissimo grazie anche alla Dr. Barbara Zaniol, che con passione mi ha "iniziato" alla spettroscopia e mi è stata vicino nella fase di setup e di analisi dati: è stata una collaborazione oltre che utile, divertente. Ringrazio anche tutti gli altri del "team di NIO" con cui ho collaborato e che hanno condiviso con me gioie dolori in questo interessante percorso.

Non posso poi esimermi dal ringraziare i miei colleghi tesisti: in primis Marta, che ha collaborato con me al medesimo esperimento, condividendo inoltre la "gelida" atmosfera della sala controllo; alla sinistra di Marta ringrazio anche Luigi, per le battute, la compagnia, i caffè e i momenti divertenti passati assieme in questi mesi; infine, ma non per questo meno imporanti, ringrazio molto i miei compagni di avventure di vecchia data, che sono stati (letteralmente) al mio fianco in questa ultima fase di scrittura, ovvero Sofia e Antonio, la vostra compagnia, l'allegria e le grasse risate, hanno reso infinitamente piacevole portare a termine questo stimolante ed interessante lavoro.

Stavo quasi dimenticando "quelli al di là del vetro", ovvero gli amici dottorandi, che ogni giorno mi chiamavano per il andare in mensa: è stato così divertente scambiarsi idee e racconti a pranzo!

Per concludere, c'è un ultimo ringraziamento che non potrei mai tralasciare: devo dire grazie a tutta la mia famiglia per essermi stata vicino e avermi sostenuto in questo percorso, in particolare ai miei genitori Annalisa e Antonio, mio fratello Manuele e mia cognata Goy (a cui vanno i miei ringraziamenti per i consigli sulla stesura e sull'inglese...).

Grazie davvero a tutti e a tutte le persone di RFX, per avere reso ancora più entusiasmante e stimolante questo semestre di tesi!